Master's Thesis

Identification of Scooping Areas in Inland Waterbodies for Touch-and-go Maneuvers of Amphibious Firefighting Airplanes using Earth Observation Data

University: *Technische Universität München*
Faculty: *Department of Aerospace and Geodesy*
Degree Program: *M.Sc. Earth Oriented Space Science and Technology*

Author: *Christoph Otto*
Student-ID: *03766517*

University Supervisor: *Prof. Dr.-Ing. Günther Strunz*
External Supervisor: *Dr. Marc Wieland*

Munich, October 25, 2024

This master thesis was elaborated at the German Remote Sensing Data Center (DFD) within the Earth Observation Center (EOC) of the German Aerospace Center (DLR) in Oberpfaffenhofen, near Munich.

Contents

Kurzfassung

Die Identifizierung geeigneter Schöpfbereiche in Binnengewässern ist für die Effizienz und Sicherheit der Brandbekämpfung aus der Luft von entscheidender Bedeutung, insbesondere angesichts der zunehmenden Schwere und Häufigkeit von Waldbränden. Amphibische Löschflugzeuge benötigen verlässliche Schöpfbereiche, um bei Touch-and-Go-Manövern die Wassertanks aufzufüllen und so eine schnelle Reaktion auf Waldbrände zu ermöglichen. Diese Arbeit untersucht die Machbarkeit der regelmäßigen, monatlichen Identifizierung solcher Schöpfgebiete mittels Erdbeobachtungsdaten unter Berücksichtigung jahreszeitlicher Schwankungen und strenger Anforderungen an Mindestlänge (2000 Meter), -breite (100 Meter), und -tiefe (drei Meter) für einen sicheren und effektiven Einsatz.

In dieser Arbeit wird die Tiefensegmentierung durch ein maßgeschneidertes Convolutional Neural Network auf der Grundlage von optischen Sentinel-2 L3A-Satellitenbildern eingesetzt, um zwischen Land und Wasser tiefer und flacher als drei Meter zu unterscheiden. Darüber hinaus wird der Scooping Area Finder for aerial fire Emergency Response (SAFER), ein speziell für diese Arbeit entwickelter Algorithmus, angewendet. SAFER nutzt den DLRS1S2-Water-Processor-Datensatz zur Erkennung von Gewässern und filtert diese effizient anhand von räumlichen Beschränkungen, den Tiefensegmentierungsergebnissen und weiteren Dimensionskriterien. Der Algorithmus identifiziert dann die am besten geeigneten Schöpfungsgebiete jedes einzelnen übrig gebliebenen Gewässers und wendet topografische Beschränkungen aus dem Copernicus Digital Elevation Model GLO-30 an, um einen zugänglichen Flugkorridor zum und vom endgültigen Schöpfungsgebiet zu gewährleisten.

Das Tiefensegmentierungsmodell erreichte eine Genauigkeitsquote von 80,7% für Gewässer, die tiefer als drei Meter sind, und eine Vollständigkeitsquote von 66,1% für flachere Gewässer, wodurch sichergestellt wird, dass geeignete tiefe Wassergebiete genau identifiziert werden, während die Einbeziehung flacher, nicht nutzbarer Gebiete minimiert wird. Bei Tests in Mecklenburg-Vorpommern und Bayern identifizierte SAFER 368 Gewässer mit einer Fläche von mehr als 0,2 km^2 in Mecklenburg-Vorpommern, von denen neun die Kriterien für geeignete Schöpfgebiete erfüllten. In Bayern wurden 246 Gewässer identifiziert, wovon 11 die Anforderungen für Schöpfgebiete erfüllten.

In der Studie werden auch die Herausforderungen beim Training des Tiefensegmentierungsmodells erörtert, insbesondere aufgrund begrenzter großräumiger Referenztiefendaten. Trotz dieser Herausforderungen zeigt der Ansatz dieser Arbeit ein großes Potenzial für eine skalierbare, genaue Identifizierung von Schöpfgebieten auf globaler Ebene, die eine Überwachung über große räumliche Ausdehnungen und in monatlichen Abständen ermöglicht. Dies liefert wertvolle Erkenntnisse für die Optimierung von Brandbekämpfungsmaßnahmen aus der Luft.

Abstract

Identifying suitable scooping areas in inland waterbodies is crucial for the operational efficiency and safety of aerial firefighting, especially in light of the increasing severity and frequency of wildfires. Amphibious firefighting airplanes require reliable scooping areas to refill water tanks during touch-and-go maneuvers, enabling rapid response to wildfires. This thesis investigates the feasibility of using Earth Observation data to identify suitable scooping areas on a monthly basis, accounting for seasonal changes and ensuring they meet strict criteria of at least 2000 meters in length, 100 meters in width, and a minimum depth of three meters for safe and effective operations.

The thesis employs depth segmentation through a custom convolutional neural network model based on Sentinel-2 L3A optical satellite imagery to distinguish between land and water deeper and shallower than three meters. It further develops and applies the Scooping Area Finder for aerial fire Emergency Response (SAFER), an algorithm created specifically for this thesis. SAFER utilizes the DLRS1S2-Water-Processor dataset to detect waterbodies, efficiently filtering them using spatial constraints, depth segmentation results, and further dimensional criteria. The algorithm then identifies the most suitable scooping areas of each remaining waterbody and applies topographic constraints from the Copernicus Digital Elevation Model GLO-30 ensuring accessible flight corridors to and from the final scooping areas.

The depth segmentation model attained a precision of 80.7% for waters deeper than three meters and a recall of 66.1% for shallower waters, ensuring that suitable deep water areas are accurately identified while minimizing the inclusion of shallow, non-viable areas. Tested in Bavaria and Mecklenburg-Vorpommern, SAFER identified 368 waterbodies larger than $0.2km^2$ in Mecklenburg-Vorpommern, of which 9 met the criteria to contain scooping areas, and 246 in Bavaria, yielding 11 waterbodies meeting the scooping requirements.

The study also discusses challenges in training the depth segmentation model, particularly due to limited large-scale reference depth data. Despite these challenges, this approach demonstrates strong potential for scalable, accurate identification of scooping areas on a global scale, allowing monitoring across large spatial extents and at monthly intervals. This provides valuable insights for optimizing aerial firefighting efforts.

List of Figures

List of Tables

List of Abbreviations

AOI Area of Interest.

BKG German Federal Agency for Cartography and Geodesy.

CNN Convolutional Neural Network.

DEM Digital Elevation Model.

DG-ECHO Directorate-General for European Civil Protection and Humanitarian Aid Operations.

DLM Digital Landscape Model.

DLR German Aerospace Center.

EO Satellite-based Earth Observation.

EU European Union.

GSD Ground sampling Distance.

IoU Intersection over Union.

km Kilometer.

LiDAR Light Detection and Ranging.

m Meter.

MAJA Multi-sensor Atmospheric Correction and Cloud Screening ATCOR Joint Algorithm.

NIR Near Infrared.

SAFER Scooping Area Finder for aerial fire Emergency Response.

SAR Synthetic Aperture Radar.

STAC Spatiotemporal Asset Catalogs.

SWIR Shortwave Infrared.

WASP Weighted Average Synthesis Processor.

WFS Web Feature Service.

1 Introduction

In recent years, the frequency and severity of wildfires across the globe have risen drastically, fueled by climate change, deforestation, and increasingly dry conditions in some regions [Cunningham et al., 2024; Jolly et al., 2015; Tyukavina et al., 2022; Global Forest Watch, 2024; FAO, 2024, pp. 8f.]. These fires not only devastate vast areas of forest and vegetation, but also result in the loss of biodiversity, the increasing health risks for humans, and the release of enormous amounts of carbon dioxide into the atmosphere [Cunningham et al., 2024; Tyukavina et al., 2022; FAO, 2024, pp. 8f.]. Given the growing wildfire threat, it has become crucial to monitor fire risk [Novo et al., 2020; Sivrikaya et al., 2024] and active fires [Nolde et al., 2020; Rösch et al., 2024] by means of satellite-based Earth Observation (EO) data [Chen et al., 2024] so that governments and firefighting services can take preventive and containment measures.

Once a wildfire has started, timely and efficient firefighting operations are critical to limiting its spread. Aerial firefighting has proven to be very effective for initially combating remote wildfires until ground-based resources reach the fire event [Plucinski, 2009]. Airborne methods offer unique advantages by providing rapid response times, and the ability to access remote areas where traditional ground-based firefighting efforts may be hindered by difficult terrain or lack of infrastructure [Dilba, 2020; Wang et al., 2021].

Figure 1.1: Canadair CL-415 during a touch-and-go maneuver (© European Union).

In addition to their operational advantages, firefighting airplanes are often deployed through international cooperation mechanisms to support regions facing large-scale wildfires. Exemplarily, the European Union (EU) coordinates such efforts through its Directorate-General for European Civil Protection and Humanitarian Aid Operations (DG-ECHO) [DG-ECHO, 2024a]. It plays a key role in facilitating coordinated disaster response across EU member states and beyond.

One of its primary tools is the EU Civil Protection Mechanism, which improves the cooperation between participating countries on civil protection [DG-ECHO, 2024b].

To address the growing threat of wildfires in Europe [DG-ECHO, 2024c; DG-ECHO and DG-JRC, 2022], amongst other disasters, the EU established RescEU as part of the EU Civil Protection Mechanism. For the 2024 wildfire season, this reserve of European capacities includes a fleet of four helicopters and 24 amphibious firefighting planes. The latter, such as the Canadair CL-415 (see figure 1.1), are specialized planes capable of scooping up to 6100 liters of water from waterbodies in a matter of seconds during a touch-and-go maneuver.

1.1 Motivation

DG-ECHO stresses the need for the frequent identification of waterbodies that are able to contain these so-called scooping areas for the amphibious airplanes of the rescEU firefighting fleet to refill their tanks during a touch-and-go maneuver. This is especially crucial in regions prone to seasonal water level changes, because the identified scooping areas must meet specific criteria, as described in the following and illustrated in figure 1.2:

1. Freshwater inland waterbodies are recommended to prioritize over saltwater / open sea water surfaces.
2. Minimum dimensions: Length 2000 meters (m), width 100m, depth 3m (including safety clearance buffers).
3. The flight corridors during approach and take-off are free of obstructions such as vegetation.

1.2 Conceptualization and Objective

Given the vast extend of applicable areas of interests (AOIs) such as whole states, countries, or even continents, and due to potential seasonal changes of dimensional characteristics of inland waterbodies, a high temporal resolution and a high spatial coverage is required for the search for suitable scooping areas for firefighting airplanes. These requirements make EO data complimented by value-adding in-situ geodata an interesting tool for the given task. In general, EO data is predestined to capture georeferenced information that finds application in a broad variety of Earth-oriented studies due to their homogeneity, and high spatio-temporal resolution and coverage on a global scale [Chuvieco, 2020, pp. 1, 13-19]. The temporal resolution for identifying scooping areas was chosen to be one month, as this time span is long enough to have enough homogeneous data available (see chapter 4), but still short enough to allow for the detection of seasonal changes of dimensional characteristics of inland waterbodies.

Hence, the objective of this thesis is the monthly EO-based identification of scooping areas in inland waterbodies that fulfill the minimum dimensional criteria of 2000m x 100m x 3m and provide free flight corridors for firefighting airplanes to refill their water tanks during a touch-and-go maneuver. Its feasibility depends on two main tasks:

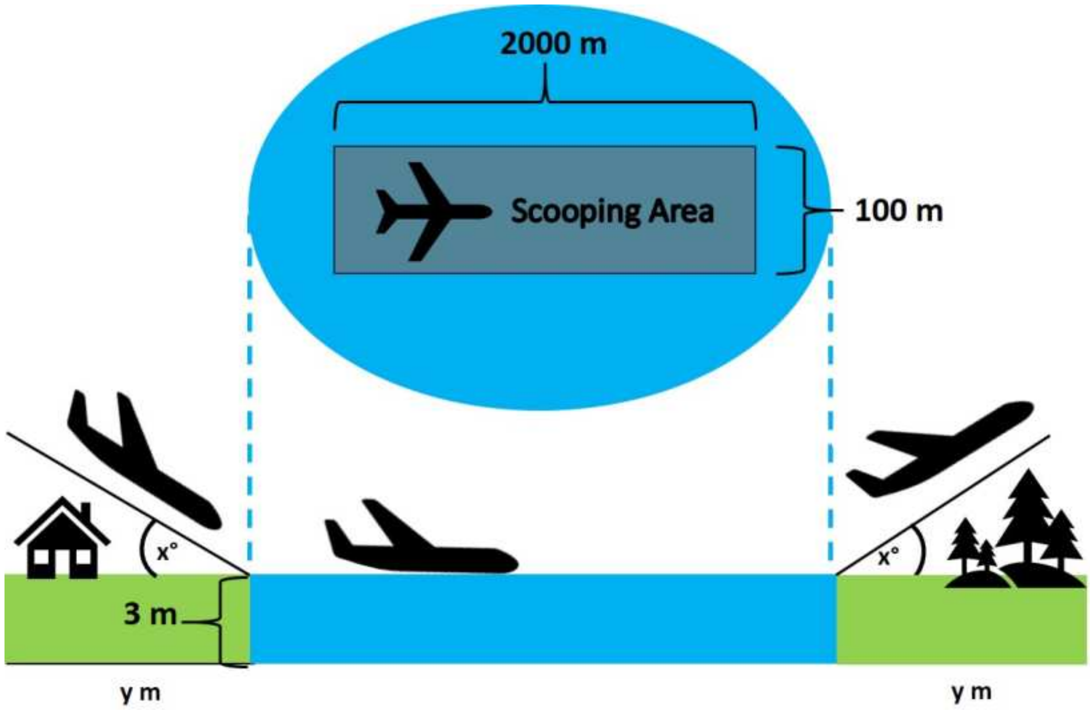

Figure 1.2: Scooping area with its minimum characteristics according to DG-ECHO. "y" denotes the length of the flight corridor that should be checked for obstructions. "x" is the attack / launch angle of the firefighting airplane.

1. Depth estimation of water surfaces of inland waterbodies deeper and shallower than a selected threshold. In the scope of this thesis, the threshold is 3m in accordance to DG-ECHO's requirements (see chapter 1.1). Only water areas deeper than 3m are eligible for scooping area locations.

2. a) Creating a scooping area finder algorithm to identify waterbodies capable of containing a scooping area as well as scooping areas itself, and b) checking if flight corridors to and from the detected scooping areas are usable for firefighting airplanes given a certain attack / launch angle.

In the scope of this thesis, point two will be realized in form of a Python software package with the option to input the result of point one in order to filter waters which are shallower than 3m. This procedure is explained in chapter 5.

1.3 Research questions

During developing and testing a methodology to fulfill the previously defined objective, it is indented to check its feasibility by answering the following research questions:

1. Using EO data and shape filtering analysis, is it possible to efficiently identify which inland waterbodies are able to contain scooping areas for firefighting airplanes?

2. Is it feasible to rank the found scooping areas per waterbody by a certain criterion to find the optimal ones?
3. Is it possible to classify water surfaces of inland waterbodies according to whether they are deeper or shallower than 3m solely based on EO data?
4. Is it practical to use height information to check if a scooping area is approachable via free flight corridors by firefighting airplanes?

2 State of Research

On one hand, several studies have investigated the efficiency of firefighting airplanes, focusing on their operational effectiveness in combating wildfires. These works explore various aspects, such as their performance and water drop strategies [Yang et al., 2024; Czyż et al., 2023; Kal'avský et al., 2019; Wang et al., 2021; Calkin et al., 2014], as well as more specialized studies like routing optimization for firefighting airplanes [Chalabi et al., 2024]. However, all of these studies assume that suitable scooping areas have already been identified prior to their analysis.

On the other hand, a variety of studies has focused on detecting and monitoring waterbodies using optical or Synthetic Aperture Radar (SAR) EO data, particularly for water surface detection and flood monitoring [Martinis et al., 2009; Landuyt et al., 2019; Bai et al., 2011; Yang et al., 2017; Xie et al., 2016; Thito et al., 2016; Cian et al., 2018], partially with the help of with neural networks [Wieland & Martinis, 2019; Wieland et al., 2024; James et al., 2021]. However, in all conscience, they have not been applied to the specific task of identifying viable scooping areas for aerial firefighting.

This thesis aims to fill that gap by using EO data to identify scooping areas across large spatial extents with high temporal resolution. This approach is unique in its integration of EO data to systematically map scooping areas which has not been attempted in previous studies. To address this research gap, depth estimation of inland waterbodies, as well as shape filtering algorithms need to be applied.

2.1 Depth Estimation of Inland Waterbodies using Earth Observation Data

Even though the global bathymetry dataset GLOBathy [Khazaei et al., 2022], providing depth estimates for over 1.4 million inland waterbodies, could theoretically be used to extract water areas deeper than 3m, its suitability for this study is limited. The depth of the inland waterbodies is estimated based on temporally static information from the HydroLAKES dataset [Messager et al., 2016] with huge margins of errors up to a root mean square error of 87.92m. In contrast, this thesis requires a more dynamic and accurate approach, with monthly updates to accurately differentiate between water shallower and deeper than 3m. As such, depth estimation based on real-life observations was deemed more appropriate in the scope of this thesis.

These real-life observations of depth or depth change can come from in-situ measurements such as ship-based echo-sounding, airborne Light Detection and Ranging (LiDAR), or satellite-based altimetry. However, these techniques are not viable for obtaining repeated depth measurements for large-scale spatial coverages due to technical limitations, unlike depth estimations based on optical EO data [Misra & Ramakrishnan, 2020; Mandlburger et al., 2021]. While optical EO data is generally only suitable for depth estimation up to 20m [Mandlburger et al., 2021], this limitation is not relevant for this thesis, as it aims to classify water areas into those deeper and shallower than 3m.

Depth estimation of water areas based on optical EO data has been taken on by many research studies. According to Misra & Ramakrishnan [2020], optical based depth estimation algorithms can be generally divided into three different approaches: physics-based models, empirical models, and machine learning-based models. In the former, radiative transfer models are inverted to reflect the way light interacts with the water's surface, the water itself, and the bottom. These models are based on physical principles. However, they are not suited for application on global scale, as physical parameters such as chlorophyll concentration and reflectance spectra need to be estimated for different regions, as done by Kerr & Purkis [2018] in five different AOIs in the Caribbean Sea. Empirical models, by contrast, use linear regression techniques to estimate depths. They rely on direct in-situ data from the study area to establish the relationship between reflectance and depth, as demonstrated by Casal et al. [2019] at the Irish coast or Traganos et al. [2018] at coastal regions in the Aegean Sea. An extension of linear empirical models is the machine learning-based models which can capture non-linear relationships between reflectance and depth, offering even higher accuracy potential [Mabula et al., 2023; Misra & Ramakrishnan, 2020; Yunus et al., 2019] and thus being frequently employed in recent studies. Lumban-Gaol et al. [2021] used Convolutional Neural Networks (CNNs) with multispectral EO data to estimate depth in shallow coastal areas around Puerto Rico, but observed that the performance of the pretrained model declined when applied to other open sea coastal regions with different water conditions. To account for different water conditions due to waves, Najar et al. [2022] came up with a novel approach that integrates satellite-derived wave kinematics with multispectral EO data as input to their CNN-based Deep Single-Point Estimation of Bathymetry model, allowing for depth retrieval up to 40m in rough coastal areas of French Guiana and France. Similarly, despite varying conditions of human activities, pollution, and sediment accretion, Wu et al. [2021] demonstrated that using diverse machine learning algorithms and optical EO data enables accurate depth estimation up to 9m in the turbid seaport environments of Nanshan, China. Agrafiotis et al. [2024] introduces MagicBathyNet, in all conscience, one of the few publicly available CNN models for depth estimation in coastal open sea areas in Cyprus and Poland for different sensors including multispectral EO data. Extending these findings to inland waterbodies, Yunus et al. [2019] showed that machine learning-based depth estimation up to 30m is also effective for lakes, where a Random Forest model using multispectral EO data achieved high accuracy in optically clear waters. Mandlburger et al. [2021] developed BathyNet, a depth segmentation CNN specifically optimized for estimating depths in shallow lakes in southern Germany from multispectral aerial images. To achieve higher accuracy, this model requires a coastal blue band with a wavelength around 430 nanometers in addition to standard RGB-channels, making it incompatible with common multispectral EO data.

All of the above mentioned studies showed that it is feasible to estimate depth of shallow waters with optical EO data. However, none of the proposed models can be directly employed as pretrained solutions for large-scale depth estimation across inland waterbodies within the scope of this thesis. This limitation arises from factors such as the non-open-source nature of some models, inconsistencies in required input data types, or incompatibility between the applicable AOIs of these models and those relevant to this thesis. Additionally, all of these studies required the input data to be clipped to the extent of water in a separate preprocessing step, adding further complexity to their application. To address these challenges, this thesis introduces a depth segmentation model based on a CNN model by Wieland et al. [2024] trained to differentiate between water and land, ensuring alignment with the specific requirements of this study.

2.2 Shape Filtering Algorithms

In addition to depth estimation, the effective identification of scooping areas in inland waterbodies requires the application of shape filtering algorithms. These algorithms play a critical role in processing the polygonal representations of waterbody shapes obtained from EO data. Shape filtering algorithms ensure that only those waterbody polygons that can definitively accommodate at least one scooping area remain for the subsequent shape fitting processes. Following this, shape fitting algorithms identify all potential locations and orientations for scooping areas within the filtered waterbody polygons. This is most intuitively achieved through a brute-force approach that iterates over various possible locations and orientations of the scooping area, as existing algorithms for 2D rectangle packing do not account for overlapping rectangles [Coffman et al., 1980; Chung et al., 1982; Berkey & Wang, 1987].

The most efficient way to filter waterbody polygons is by finding the largest inscribed rectangle with arbitrary orientation within the waterbody polygon. If the dimensions of this rectangle are too small for a scooping area, the respective waterbody is omitted. Many studies focus on the concept of largest inscribed rectangles. However, most primarily search for axis-aligned rectangles instead of ones with arbitrary orientation [Marzeh et al., 2019; Sarkar et al., 2018; Daniels et al., 1997]. This thesis requires the use of arbitrary rectangles because scooping areas do not need to be aligned with the coordinate axes, rather, their orientation can vary depending on the specific characteristics of the waterbody. In this context, a distinction is often made between convex [Knauer et al., 2012] and concave polygons [Knauer et al., 2012; Molano et al., 2012]. A convex polygon is a geometric figure where all interior angles are smaller than 180 degrees. In contrast, a concave polygon has at least one interior angle greater than 180 degrees, creating an outward bulge. Since the waterbody polygons represent real-life water surfaces with potential islands, it is essential to utilize an algorithm capable of finding the largest inscribed rectangle with arbitrary orientation within a concave polygon with potential holes. However, the computational cost is dependent on the number of vertices. In all conscience, [Knauer et al., 2012] is the study that approximates the largest inscribed rectangle with arbitrary orientation within a concave polygon with potential islands with the lowest computational cost of $O(\frac{1}{\epsilon}n^3log^2n)$, where n represents the number of vertices of the polygon and ϵ is the approximation parameter. Notably, setting $\epsilon = 0$ yields the exact largest inscribed rectangle. However, implementing this algorithm within the context of this thesis would incur excessive computational costs, as waterbody polygons typically possess a high number of vertices due to their natural shapes and large sizes. Therefore, this thesis employs a workflow that filters waterbody polygons by calculating the minimum rotated bounding box (colloquially referred to as the minimum "outscribed" rectangle) for each waterbody and comparing its dimensions to those of a scooping area. While this approach may mean that not all remaining waterbody polygons can accommodate at least one scooping area for subsequent shape fitting processes, it significantly reduces the computational cost to $O(nlogn)$ [The Infinite Loop, 2014; Medium, 2020].

3 Area of Interest

The methodology of this thesis allows to define the AOI anywhere in the world (see chapter 5). However, to be able to properly develop and test the methodology of the search for scooping areas, the German states Mecklenburg-Vorpommern and Bavaria were selected as initial AOIs (see figure 3.1). They offer diverse topographies rich in inland waterbodies with the former state being mostly flat, and the latter showing mostly mountainous characteristics, especially in its alpine region in the south. Furthermore, Germany offers open access to a great amount of geodata that is used in this thesis (see chapter 4).

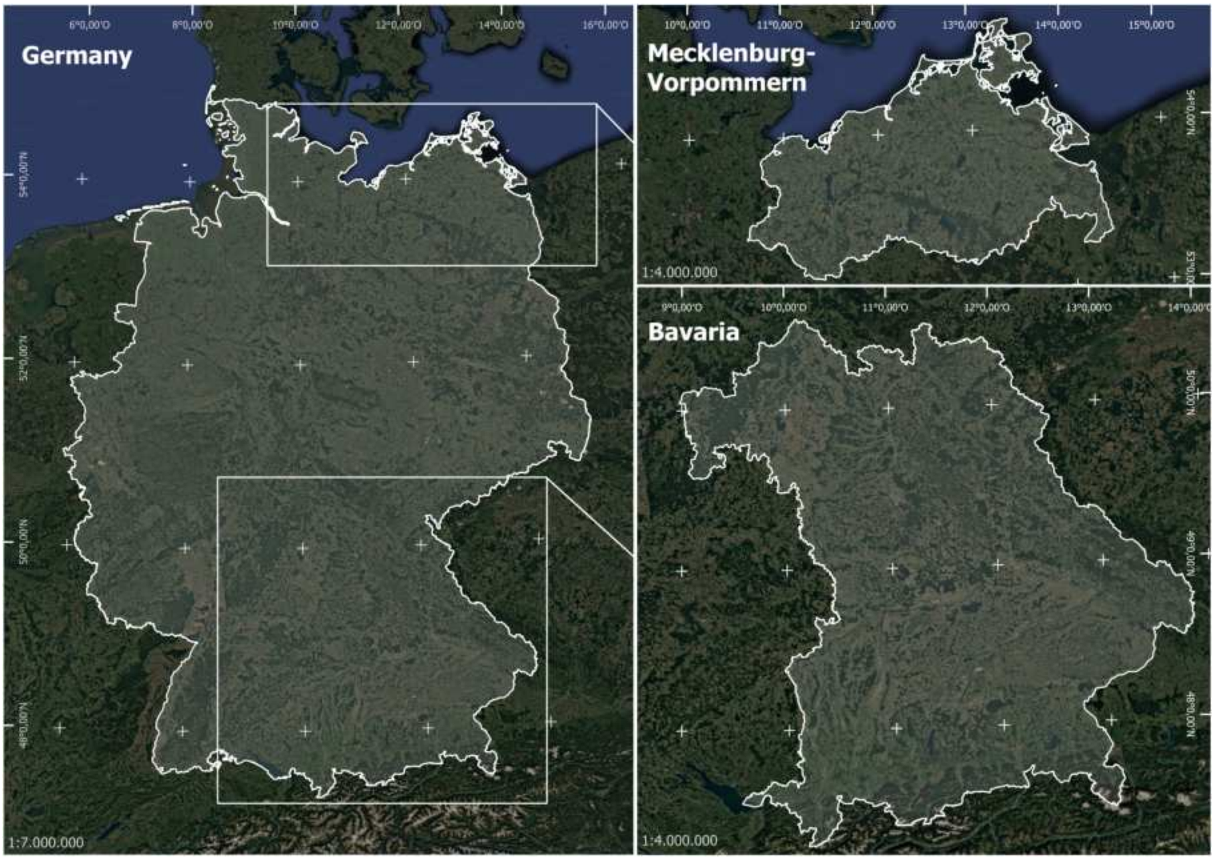

Figure 3.1: Area of interest

4 Data

In the following, the data used to achieve the objective outlined in chapter 1.2 are presented. They are divided into data that are used for depth segmentation, and data that are used for the scooping area identification.

4.1 Data for Depth Segmentation

The following datasets are used to segment water surfaces of inland waterbodies according to whether the water is deeper or shallower than 3m by the means of a supervised machine learning model, for which training and reference data are needed.

4.1.1 Depth maps of the lakes in Mecklenburg-Vorpommern

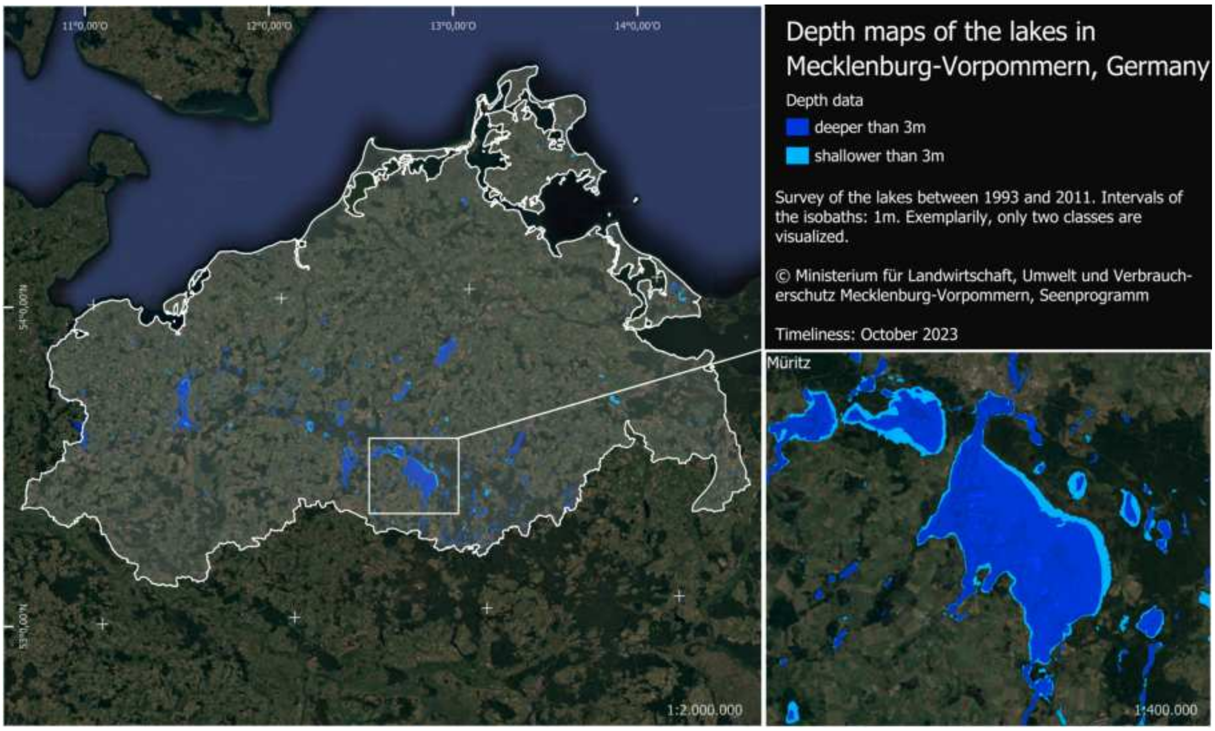

Figure 4.1: Visual presentation of the depth maps of the lakes in Mecklenburg-Vorpommern.

This dataset contains polygons indicating the depth of 95% of all waterbodies in the German state Mecklenburg-Vorpommern, excluding fish farms and temporary waterbodies. The polygons were created by interpolated isobaths with an interval of 1m. The isobaths are based on differential global positioning system and echo sounding surveys between the years 1993 and 2011 [Ministerium für Landwirtschaft, Umwelt und Verbraucherschutz M-V, Seenprogramm, 2023].

In the scope of this thesis, the dataset is used as reference for the depth segmentation because it is, in all conscience, one of the few openly available depth datasets for inland waterbodies whose spatial coverage falls into the AOI (see chapter 3) and whose depth resolution is as low as 1m. The latter property makes it possible to aggregate the dataset into water surfaces shallower and deeper than the required 3m. The dataset was downloaded via the Web Feature Service (WFS) `https://www.umweltkarten.mv-regierung.de/script/mv_a3_gewaesser_wfs.php?` (accessed: 2024-10-25) using QGIS. Figure 4.1 visualizes the data aggregated to the two depth classes needed in the scope of this thesis.

4.1.2 Sentinel-2 MSI Level 3A (MAJA/WASP Tiles) for Germany

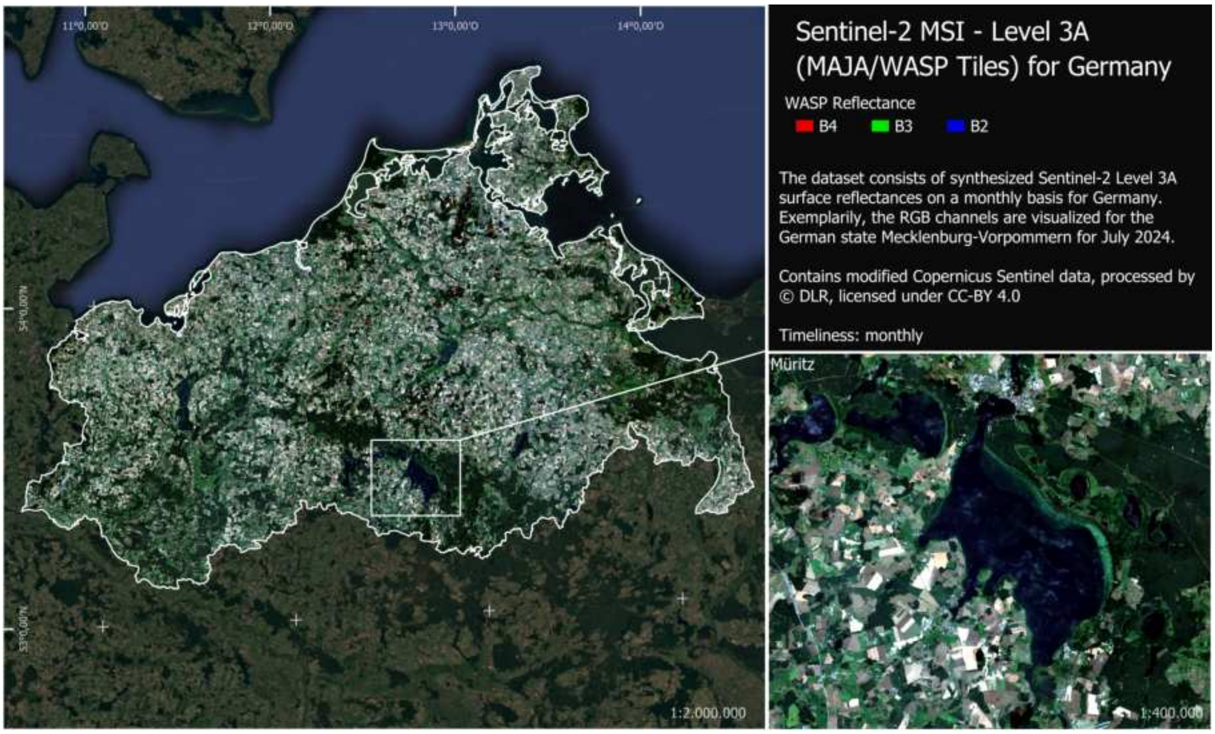

Figure 4.2: Visual presentation of the Sentinel-2 MSI Level 3A (MAJA/WASP Tiles) for Germany.

Sentinel-2 is a multi-spectral imaging mission within the EU's EO program called Copernicus consisting of twin satellites. The mission has a revisit frequency of five days and maps the Earth with a swath width of 290 kilometers (km). Sentinel-2 obtains reflectances in 13 spectral bands with a ground sampling distance (GSD) of up to 10m. The raw data is usually preprocessed to the so-called Sentinel-2 L1C tiles, consisting of radiometric and geometric corrected, orthorectified top-of-atmosphere reflectances [Copernicus, 2024c].

The Sentinel-2 MSI L3A (MAJA/WASP Tiles) for Germany dataset is the result of Sentinel-2 L1C tiles being processed at first by the Multi-sensor Atmospheric Correction and Cloud Screening ATCOR Joint Algorithm (MAJA) to Sentinel-2 L2A tiles with surface reflectances, and afterwards being processed by the Weighted Average Synthesis Processor (WASP) to synthesized, monthly aggregated Sentinel-2 L3A surface reflectances in Germany [Earth Observation Center of the German Areospace Center, 2024]. These two processing steps are shortly explained in the following.

For each Sentinel-2 L1C tile, MAJA estimates aerosol optical thickness and water vapour in the atmosphere, applies an atmospheric correction to obtain surface reflectances, and creates masks for clouds and their shadows. Next, WASP aggregates all the Sentinel-2 L2A tiles from MAJA within a synthesis period of 45 days to obtain cloud-free Sentinel-2 L3A surface reflectances for each month. WASP does this by firstly homogenising the MAJA surface reflectances with a directional correction as if they had been measured with a vertical viewing angle. This correction is needed to merge reflectances from overlapping sensor orbits which is the case for Sentinel-2. In these overlaps, surface reflectances are measured by different viewing angles depending on the orbit of the sensor creating different surface reflectances for the same location. Secondly, the aggregation of the surface reflectances over a synthesis period of 45 days is done by a weighted average for each pixel and each band in the homogenised MAJA tiles. The weights for pixels are lower the closer they are to clouds or their shadows, the higher the aerosol optical thickness is, and the larger the temporal distance is between the pixel's date and the middle date of the synthesis period [Séries Temporelles, 2024].

The Sentinel-2 MSI L3A (MAJA/WASP Tiles) for Germany dataset is chosen as training data for the depth segmentation due to its following properties:

- The dataset's spatial coverage completely covers the AOI of this thesis (see chapter 3).
- The dataset has a temporal resolution of one month, which aligns with the objective of this thesis (see chapter 1.2).
- Sentinel-2 MSI L3A already contains cloud- and shadow-free surface reflectance values so that no atmospheric, radiometric and geometric corrections are necessary as preprocessing steps.

The data needed in the scope of this thesis was accessed from the Spatiotemporal Asset Catalogs (STAC) library `https://geoservice.dlr.de/eoc/ogc/stac/v1/collections/S2_L3A_WASP` (accessed: 2024-10-25) of the Earth Observation Center of the German Aerospace Center DLR. The dataset is visualized in figure 4.2.

4.2 Data for Scooping Area Identification

The following data is used for the identification of suitable scooping areas based on their planar dimensions and their flight corridor.

4.2.1 DLRS1S2-Water-Processor

The DLRS1S2-Water-Processor dataset, visualized in figure 4.3, is a binary water mask (0 for land, 1 for water) with a GSD of 10m computed for each available Sentinel-1 GRD IW and Sentinel-2 L1C image, including meta data such as maximum cloud cover.

Sentinel-1 is, similar to Sentinel-2 (see chapter 4.1.2), a twin satellite mission within the EU's Copernicus program with a six day repeat cycle. However, unlike Sentinel-2, it performs C-band

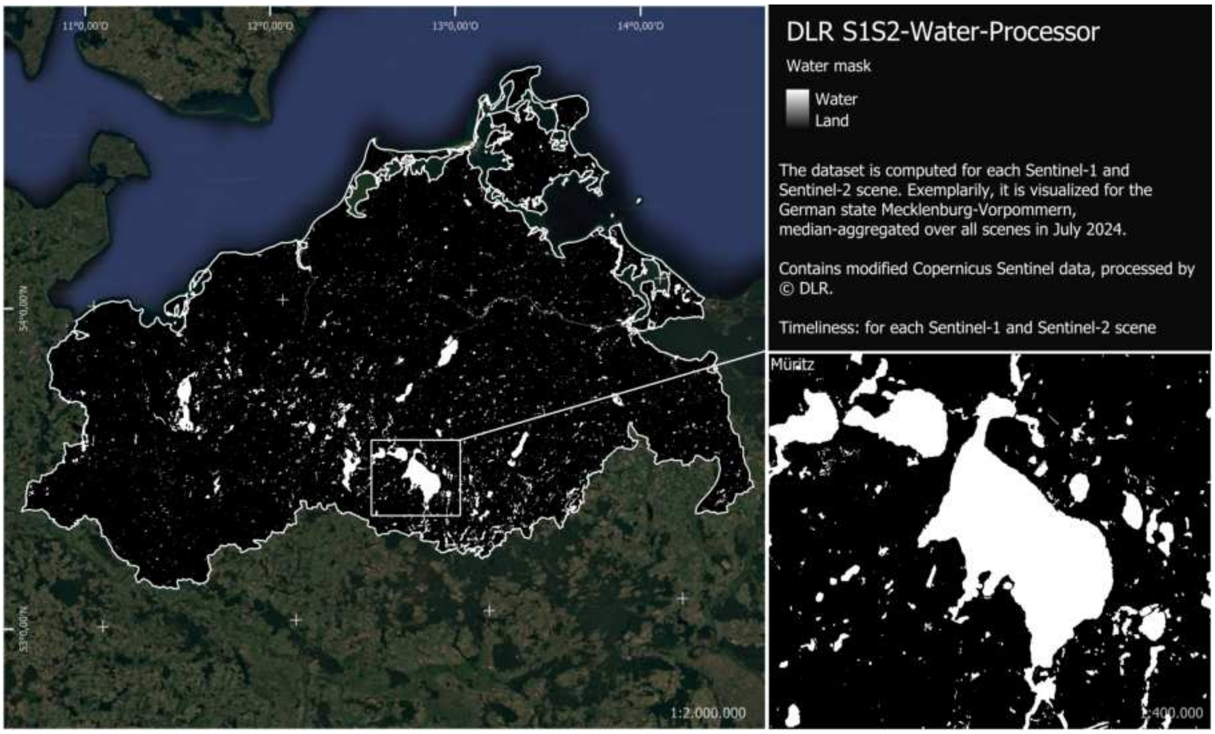

Figure 4.3: Visual presentation of the DLRS1S2-Water-Processor data.

SAR imaging with a GSD down to 5m and a swath width up to 400km depending on the acquisition mode [Copernicus, 2024c]. The Sentinel-1 GRD IW images used as input for the DLRS1S2-Water-Processor dataset have a GSD of 10m and are mapped in the IW mode.

The DLRS1S2-Water-Processor dataset is the output of two CNN models developed by Wieland et al. [2024], one trained for SAR data input such as Sentinel-1 scenes (from now on called *DLRS1-Water-Processor* model), and the other trained for optical data input such as Sentinel-2 scenes (from now on called *DLRS2-Water-Processor* model). These two CNN models showed the best performance in a comparison of different U-Net architecture CNN models for the semantic segmentation of waterbodies. Their architecture and training is briefly explained in the following.

To uniformly train the different U-Net architecture CNN models and make their performance comparable, Wieland et al. [2024] created a global benchmark dataset for semantic segmentation of waterbodies from Sentinel-1 and Sentinel-2 scenes, called S1S2-Water. It consists of 65 samples spread across diverse land cover types, aligned to the Sentinel-2 tile grid with a GSD of 10m. Each sample consists of a Sentinel-1 GRD IW image, a Sentinel-2 L1C image constrained to 5% maximum cloud cover, an elevation and slope layer, both derived from the Copernicus Digital Elevation Model (DEM) GLO-30 (see chapter 4.2.2), and a valid pixel mask indicating pixels for which a valid prediction can be made. For the Sentinel-1 GRD IW image, the VV and VH polarizations were stored in separate bands. For sentinel-2 L1C, the three visible bands Red, Green, and Blue, as well as the Near Infrared (NIR) and the two Shortwave Infrared (SWIR) bands were used [Wieland et al., 2024].

For the training of the different U-Net architecture CNN models, the generated S1S2-Water benchmark dataset was divided into training, validation and test sets, standardized based on the training set, and split into tiles of 256 x 256 pixels. The two ultimately selected CNN models for the DLRS1S2-Water-Processor dataset consist both of a EfficientNet-B0 encoder and a U-Net decoder. They are each trained with an initial learning rate of 1e-3 with a step-wise reduction by a factor of 0.1 after three epochs without improvements, a weight decay of 1e-2, an AdamW optimizer, an equally weighted combination of cross-entropy and Lovász loss optimizing the Intersection over Union (IoU) to account for class imbalance, and a batch size of 64, to name a few hyperparameters. The prediction probabilities between 0 and 1 in the last layer were turned into 1 for logits higher than or equal to 0.5, indicating water. Else, 0 indicating land is set as output class. Furthermore, the comparison showed that the best training results were obtained by augmenting the training set increasing its variability with vertical flips, scaling and cropping, and adjustments to the brightness and the contrast. The *DLRS1-Water-Processor* model achieved the best results using the VV and VH polarization bands from the Sentinel-1 GRD IW images together with the slope layer as input bands with an IoU of 0.838, a precision of 0.954, and a recall of 0.877. The *DLRS2-Water-Processor* model meanwhile achieved the best results using the Red, Green, Blue, and NIR bands from the Sentinel-2 L1C image, also together with the slope layer but excluding the two SWIR bands, scoring an IoU of 0.962, a precision of 0.991, and a recall of 0.974 [Wieland et al., 2024].

The currently operating processing pipeline of the DLRS1S2-Water-Processor dataset asks for sole input either for a Sentinel-1 GRD IW image with VV and VH polarization bands making use of the *DLRS1-Water-Processor* model, or a Sentinel-2 L1C image with Red, Green, Blue, NIR, SWIR1, and SWIR2 bands making use of the *DLRS2-Water-Processor* model. Even though the inclusion of the latter two bands of a Sentinel-2 L1C image provided slightly worse performance metrics during the training of the *DLRS2-Water-Processor* model, they are included in the DLRS1S2-Water-Processor dataset processing pipeline to obtain better atmospheric transparency in optical images with higher cloud cover due to their longer wavelength in comparison to the visible bands. Wieland et al. [2024] suggested that the slightly worse performance metrics during the training were caused by S1S2-Water not containing Sentinel-2 L1C images with cloud cover larger than 5%. Hence, the benefits of using the two SWIR bands for differentiating land and water in optical images with high cloud cover were not exploited. The slope layer used during training is automatically added from the Copernicus DEM GLO-30 (see chapter 4.2.2) in the processing pipeline for both the Sentinel-1 GRD IW image and the Sentinel-2 L1C image.

The DLRS1S2-Water-Processor dataset is used to identify the waterbodies that are eventually further processed to check if scooping areas will fit in them. The dataset tiles are stored in and accessed from an internal DLR Earth Observation Center STAC library.

4.2.2 Copernicus Digital Elevation Model GLO-30

The Copernicus DEM GLO-30 is a Digital Surface Model meaning that it represents the surface of the Earth including vegetation and infrastructure with a GSD of 30m. The maximum absolute vertical accuracy is given with 4m. The maximum relative vertical accuracy is given with 2m for slopes below or equal 20%, and 4m for slopes above 20%. The data was acquired by the TanDEM-X mission between 2011 and 2015 [Copernicus, 2024a].

The height information of the DEM is needed to check if the flight corridor to and from the eventually identified scooping areas is free. Its tiles were provided by the same internal DLR

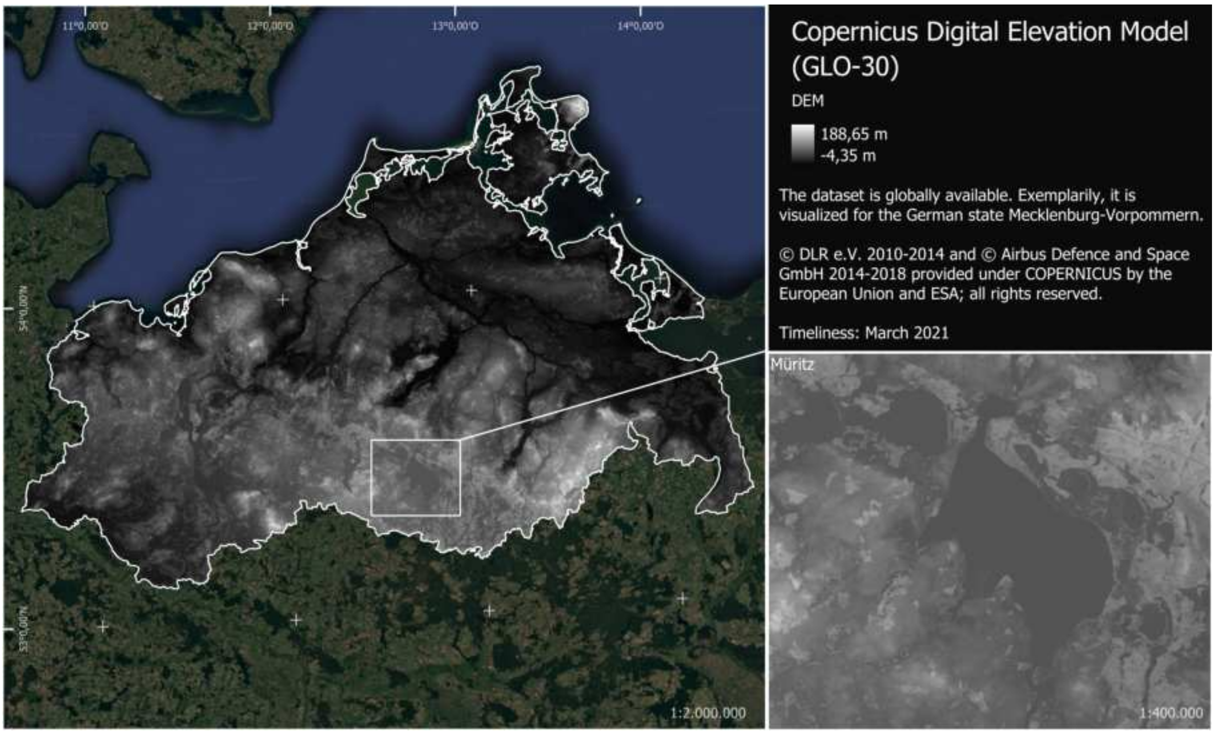

Figure 4.4: Visual presentation of the Copernicus DEM GLO-30.

Earth Observation Center STAC library in which the DLRS1S2-Water-Processor dataset is stored (see chapter 4.2.1). The dataset is visualized in figure 4.4.

4.2.3 Digital Landscape Model 250

The Digital Landscape Model (DLM) 250 describes the topographic landscape objects in Germany such as infrastructure, settlement and vegetation in vector format with 100m positional accuracy and is provided by the German Federal Agency for Cartography and Geodesy BKG [German Federal Agency for Cartography and Geodesy, 2024]. Nevertheless, in the scope of this thesis, only the following layers are used:

GEB03 contains protected areas such as nature reservoirs as polygons.

VER01 contains road traffic such as highways as line strings.

VER02 contains paths such as country roads as line strings.

VER03 contains railway traffic as line strings.

VER06 contains transport buildings and facilities such as dams or bridges as line strings.

The layers needed in the scope of this thesis, as illustrated in figure 4.5, were downloaded from the BKG's website `https://gdz.bkg.bund.de/index.php/default/digitales-landschaftsmodell-1-250-000-ebenen-dlm250-ebenen.html` (accessed: 2024-10-25), which are illustrated in figure 4.5.

The layers are used to filter identified waterbodies inside protected areas and detect water-crossing infrastructure that influences the location of scooping areas. It is dependent on the choice of the AOI, meaning that the data is only locally available in the AOI presented in chapter 3. In case scooping areas shall be identified in an AOI outside of Germany and the use of value-adding in-situ data is considered meaningful, the DLM needs to be replaced with a similar dataset according to the bounds of the new AOI. In chapter 7.1.4, alternative data is suggested.

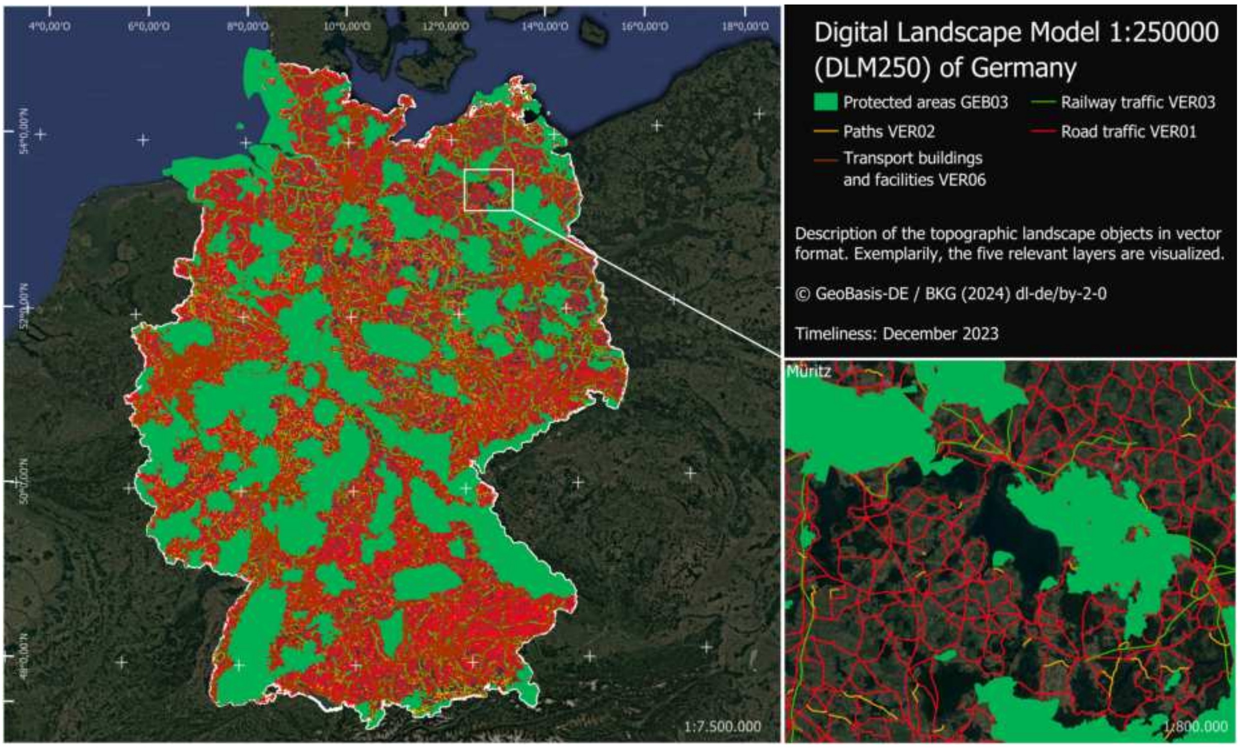

Figure 4.5: Visual presentation of selected layers of the DLM250.

5 Methodology

In the following, the methodology for this thesis' objective, namely the monthly EO-based identification of scooping areas in inland waterbodies that fulfill the minimum dimensional criteria of 2000m x 100m x 3m and provide free flight corridors for firefighting airplanes to refill their water tanks during a touch-and-go maneuver, is elaborated.

In a first step, a depth segmentation of water surfaces of inland waterbodies deeper and shallower than 3m is performed, as only the former water surfaces are eligible for scooping areas. This procedure is described in chapter 5.1. Secondly, the segmentation results serve as input to the actual search for scooping areas with free flight corridors by means of a custom scooping area finder algorithm. In the scope of this thesis, this algorithm was developed from scratch for the specific use case of identifying scooping areas in the form of a Python package called Scooping Area Finder for aerial fire Emergency Response, or abbreviated SAFER. The methodology of SAFER is explained in chapter 5.2. The overall methodology is visualized in figure 5.1.

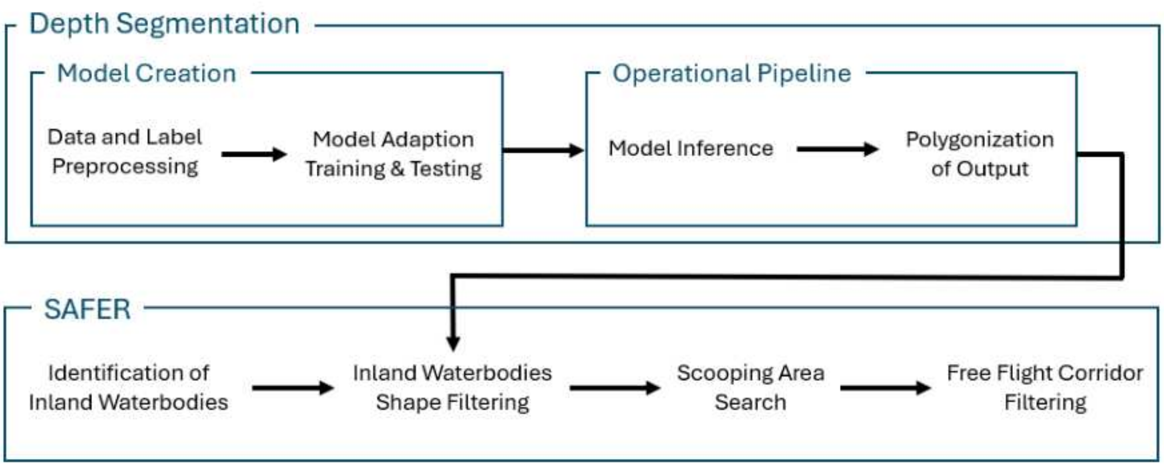

Figure 5.1: Overview of the methodology.

5.1 Depth Segmentation

As already outlined in chapter 1.2, the goal of the depth segmentation is to distinguish water surfaces of inland waterbodies deeper and shallower than 3m. The depth segmentation is carried out by a CNN model that uses optical EO data as input and outputs one of three classes per pixel: *land*, *water shallower than 3m*, and *water deeper than 3m*. The model architecture and its training is closer described in chapter 5.1.1. As training data, the Sentinel-2 MSI L3A (MAJA/WASP Tiles) for Germany dataset (see chapter 4.1.2) is used with the Red, Green, Blue, NIR, SWIR1, and SWIR2 bands. The depth maps of the lakes in Mecklenburg-Vorpommern dataset (see chapter 4.1.1), for which all depth areas shallower than 3m and deeper than 3m were dissolved, respectively, serves as reference data for the supervised learning approach of the CNN model.

5.1.1 Model Creation

The depth segmentation model is a slightly modified version of the DLRS2-Water-Processor model (see chapter 4.2.1 and Wieland et al. [2024]). It is assumed that the knowledge of the DLRS2-Water-Processor model, the segmentation of waterbodies, can be transferred to perform depth segmentation by increasing the number of output classes from two to three, namely *land*, *water shallower than 3m*, and *water deeper than 3m*.

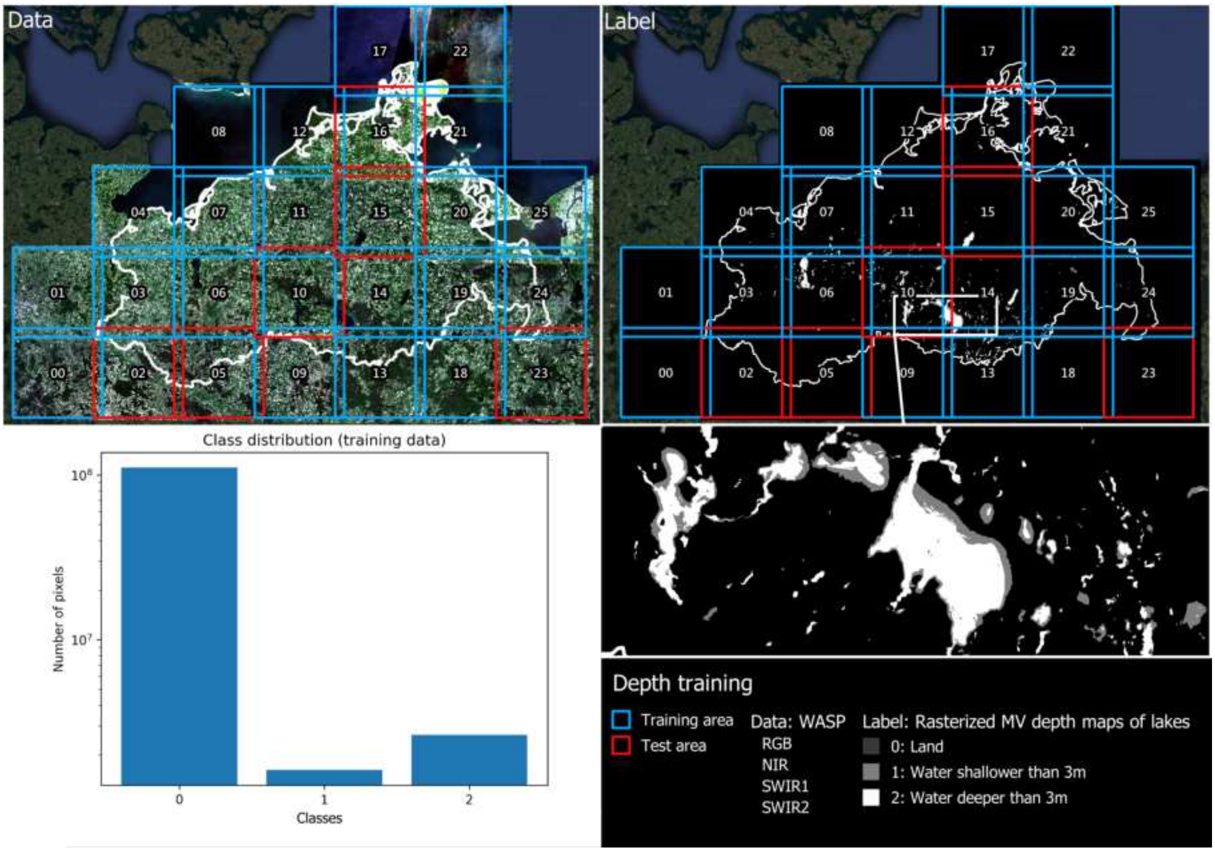

Figure 5.2: The upper left image shows the Sentinel-2 MSI L3A (MAJA/WASP Tiles) for Germany dataset cropped to tiles that form a grid covering Mecklenburg-Vorpommern. The upper right image shows the rasterized depth maps of the lakes in Mecklenburg-Vorpommern dataset, cropped to the same grid tiles. The blue grid tiles are used for training, the red ones are used for testing. In the bottom left graphic, the class distribution of the training grid tiles are shown.

For training the model, a tile grid was created covering Mecklenburg-Vorpommern, the AOI in which the reference dataset is available. The tiles were randomly split into 75% tiles used for training and 25% tiles used for testing. For each tile grid extent, the training data was downloaded for May 2018. At the time of conducting the methodology, this was the date closest to the creation date of the depth maps of the lakes in Mecklenburg-Vorpommern dataset for which the Sentinel-2 MSI L3A (MAJA/WASP Tiles) for Germany dataset is available. The discrepancy between the creation date of training and reference data is addressed in chapter 7.3. Now, for each training data tile, the references covered by that tile were rasterized by setting pixels to 1 for *water shallower than 3m*, 2 for *water deeper than 3m*, and 0 for the background (*land*). Furthermore, for each tile, a valid pixel mask was created to only allow pixel segmentation inside the AOI as some tiles only partially cover Mecklenburg-Vorpommern. Both the training data as well as the reference data are visualized in figure 5.2.

The adjusted DLRS2-Water-Processor model was initialized in unfrozen state with the same weights as the original DLRS2-Water-Processor model. The retraining was done with a low initial learning rate so as not to deviate too much from the original core task.

5.1.2 Operational Pipeline

The processing pipeline of the depth segmentation is based on the processing pipeline of the DLRS1S2-Water-Processor dataset (see chapter 4.2.1), meaning that the input data is still enhanced by slope information from the Copernicus DEM GLO-30. However, the original pipeline is extended by an additional step which polygonizes the three-class-output raster to vector data indicating water areas with a depth shallower and deeper than 3m, respectively. The latter eventually serves as input to SAFER.

5.2 Scooping Area Finder for aerial fire Emergency Response

SAFER combines the shape filtering algorithm for the search for scooping areas in identified waterbodies with the check for a free flight corridor to and from the scooping area in a custom Python package. For having visual guidance during the elaboration of the components and the workflow of SAFER, it is executed for a small region in Müritz, Mecklenburg-Vorpommern (see figure 5.3), which includes all effects covered by SAFER.

5.2.1 Identification of Inland Waterbodies

The first step of SAFER is the identification of waterbodies. All the principle variables needed in this step are described below.

AOI: Vector file containing either a polygon geometry or multiple polygon geometries in form of a grid with overlapping tiles covering the entire AOI.

Date: The date indicates the year and the month in which the search for scooping areas is performed.

Scooping area width: This is the length of the shorter side of the scooping area. In the scope of this thesis, it defaults to 100m.

Scooping area length: This is the length of the longer side of the scooping area. In the scope of this thesis, it defaults to 2000m.

Water mask GSD: Pixel size of the generated water mask.

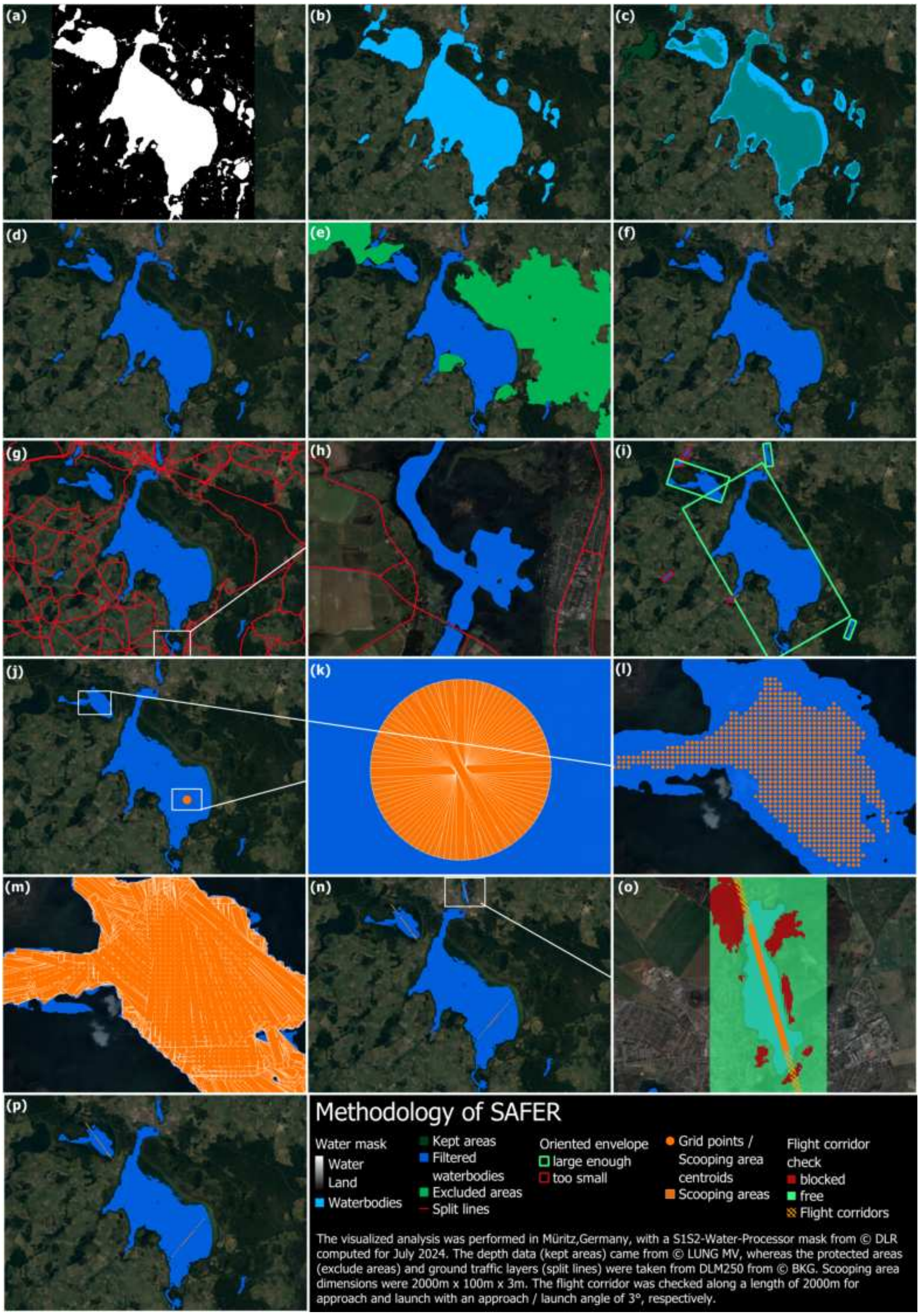

Figure 5.3: Methodology of SAFER. a) Waterbody identification; b) Polygonization of a); c) Overlay with keep areas; d) Intersection of b) and keep areas; e) Overlay with exclude areas; f) d) clipped with exclude areas; g) Overlay with split lines; h) Split applied; i) Minimum oriented bounding box filter; j) Categorizing waterbodies by distance of point of inaccessibility to their boundary; k) Scooping areas in point of inaccessibility; l) Grid over waterbody whose point of inaccessibility is too close to its boundary; m) Scooping areas found in l); n) Best scooping area per remaining waterbody; o) Free flight corridor check; p) Final output.

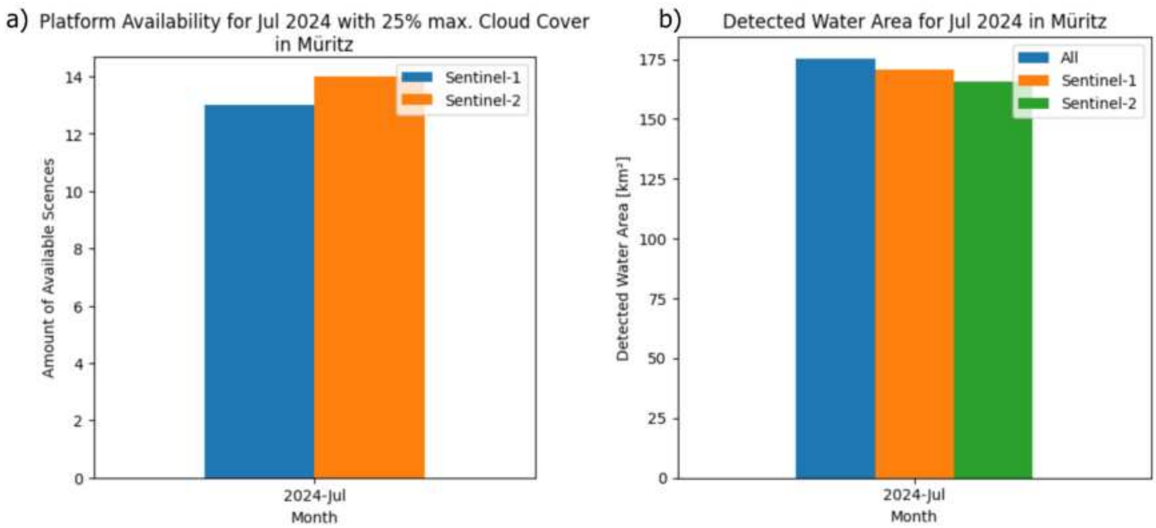

Figure 5.4: For a small AOI in Müritz in Mecklenburg-Vorpommern in July 2024, in a), the amount of tiles per platform are visualized, and in b), the detected water area per platform and combined is shown.

For the chosen *AOI* and *date*, all DLRS1S2-Water-Processor tiles, based on both Sentinel-1 and Sentinel-2 with a maximum cloud cover of 25%, are loaded from the internal DLR STAC library (see chapter 4.2.1). The choice of using tiles based on both Sentinel-1 and Sentinel-2, as well as the choice of the maximum cloud cover is justified in chapter 7.1.1. For the chosen *date* and cloud cover, 13 Sentinel-1 and 14 Sentinel-2 tiles covering the given AOI were found (see figure 5.4a. All these tiles are temporally aggregated by the median to obtain a monthly water mask with a GSD defined by the parameter *water mask GSD*. The detected water area after the temporal aggregation using all tiles and only tiles based on Sentinel-1 and Sentinel-2, respectively, is visualized in figure 5.4b. The monthly aggregation of all tiles, based on both Sentinel-1 and Sentinel-2, helps to reduce possible false segmentations within the DLRS1S2-Water-Processor dataset. The result of the binary raster-based, temporally aggregated water mask can be seen in figure 5.3a. Next, all clusters indicating water surfaces in the resulting raster that are larger than *scooping area width* $\times$ *scooping area length* (in the scope of this thesis 0.2 km^2) are polygonized so that the waterbodies can be easier filtered by dimensional and planar characteristics. The result is visualized in figure 5.3b.

5.2.2 Inland Waterbodies Shape Filtering

The next step involves the filtering of the polygonized waterbodies. The filtering is needed to omit all waterbodies whose shape is not able to contain a scooping area before starting the search for scooping areas. The filtering techniques can be split into data-dependent and data-independent filters. The former are filters the user can control with input data, the latter are integrated filters that are applied no matter the user input. All the principle variables needed for the data-dependent filters are described below.

Keep areas: : Only areas inside these polygon geometries are used for the search for scooping areas, e.g. water areas deeper than 3m. In case no *keep areas* are defined, SAFER searches in all identified waterbodies for scooping areas, independent of the depth. In the scope of this thesis, the *keep areas* are either defined by the depth maps for lakes in Mecklenburg-Vorpommern dataset (see chapter 4.1.1) for AOIs in Mecklenburg-Vorpommern or the output of the depth segmentation (see chapter 5.1).

Exclude areas: If these areas are explicitly defined, they are excluded from the search for scooping areas. In the scope of this thesis, the *exclude areas* are defined by the nature reserves and protected areas in layer GEB03 from the DLM250 dataset.

Split lines: The identified waterbodies are split by these lines into separated polygons before the search for scooping areas. This can be useful to identify water-crossing infrastructure such as bridges that are not recognized by the water mask. In the scope of this thesis, the layers VER01 (road traffic), VER02 (paths), VER03 (railways), and VER06 (transport infrastructure) from the DLM250 dataset are used as *split lines*.

At first, all the data-dependent filters depending on the above mentioned principle variables are applied. Each of these filters is followed by the data-independent filter omitting all remaining polygons smaller than 0.2 km^2.

1. The polygonized waterbodies are overlaid by the *keep areas* (see figure 5.3c) and cropped to their shape (see figure 5.3d).
2. The *exclude areas* are laid over the cropped waterbodies (see figure 5.3e) and excluded from them (see figure 5.3f).
3. Thirdly, the remaining cropped waterbodies are overlaid by the *split lines* (see figure 5.3g) and split by them (see figure 5.3h).

In the second step, all data-independent filters are practiced.

1. All remaining polygons smaller than 0.2 km^2 are omitted. This step is necessary in case none of the data-dependent filters are applied beforehand.
2. For each of the remaining cropped waterbodies, the minimum rotated rectangle, which is the minimum oriented bounding box, is calculated (visualized in figure 5.3i). In case the side lengths of the minimum rotated rectangle do not meet the dimensional criteria of the scooping area (smaller side length is smaller than the *scooping area width* or the larger side length is smaller than the *scooping area length*), these waterbodies are omitted.

After the previous filter mechanisms, all the omitted waterbodies are definitely not able to contain a scooping area, while the remaining waterbodies serve as AOI for the scooping area search.

5.2.3 Scooping Area Search

As there are infinite possibilities to fit a scooping area inside one of the remaining waterbody polygons, this thesis presents an efficient grid-based iterative shape fitting algorithm by trying different locations and rotations of a scooping area to find a finite number of best scooping areas. The thesis applies the criterion the further the scooping area is from the waterbody's boundary, the better the scooping area is rated. All the principle variables needed in this step are described below.

dTranslation: This hyperparameter influences the thoroughness of the search for scooping areas. It is the spacing between the points in north-south and west-east alignment inside the waterbody polygon that are assumed to be scooping area centroids. If this hyperparameter is divided in half, the scooping area search runtime will increase by a factor of four, but more scooping areas might be found per waterbody. In the scope of this thesis, *dTranslation* is set to 30m.

dRotation: This hyperparameter also defines the thoroughness of the search for scooping areas. It is the spacing between the azimuthal rotations of the scooping area, which are attempted between 0° and 180° for each scooping area's centroid. 0° indicates a scooping area orientation along the north-south axis, 90° indicates a scooping area orientation along the west-east axis. Due to the symmetry of the scooping area, an azimuthal rotation between 180° and 360° is not required. If this hyperparameter is divided in half, the scooping area search runtime will increase by a factor of two, but more scooping areas might be found per waterbody. In the scope of this thesis, the *dRotation* is set to 4°.

N: This number defines the maximum number of best scooping areas that are returned per waterbody. If N is higher than the number of identified scooping areas for a certain waterbody, all of its scooping areas are returned. It defaults to one, returning only the single best scooping area per waterbody.

In order to drastically reduce the runtime of the iterative brute-force search, the remaining waterbodies were split into two categories according to the minimum distance of their point of inaccessibility to their boundary. This point is the point furthest from the boundary of the waterbody. The use of this approach is discussed in chapter 7.1.2.

If the point of inaccessibility is further from the boundary than the half of the diagonal of a scooping area (in the scope of this thesis 1001.25m), it guarantees that a scooping area using the point of inaccessibility as its centroid will fit inside the waterbody polygon, no matter its azimuthal orientation. In waterbodies whose point of inaccessibility fulfills the above mentioned distance criterion (within the chosen AOI, only applicable for the large waterbody in the center of figure 5.3j), the search for scooping areas is confined to the point of inaccessibility. There, all the scooping areas with different azimuthal orientations between 0° and 180° (spacing dependent on *dRotation*) are saved (see figure 5.3k).

For waterbodies whose point of inaccessibility is less than half of the diagonal of a scooping area (in the scope of this thesis 1001.25m) from the waterbody's boundary, there is no guarantee that a scooping area will be found after its iterative rotation. Therefore, the scooping area must be iteratively translated in a dense point grid covering the whole extent of a waterbody, whereat each point serves as scooping area centroid. The density of the point grid is determined by *dTranslation*. Before the translational iteration, the point grid is purged from points that are outside the waterbody or less than half of the *scooping area width* (in the scope of this thesis 50m) from the boundary. The purged points are mathematically not able to be centroids for scooping areas that fit inside the waterbody. Next, for each grid point as scooping area centroid, all the scooping areas with different azimuthal orientations between 0° and 180° (spacing dependent on the *rotation spacing* hyperparameter) are attempted to fit inside the waterbody. Those that do fit inside, are saved. To exemplarily visualize the above mentioned step, all the scooping area centroids and scooping areas that fit inside one of the applicable waterbodies in the chosen *AOI* are shown in figure 5.3l and 5.3m, respectively.

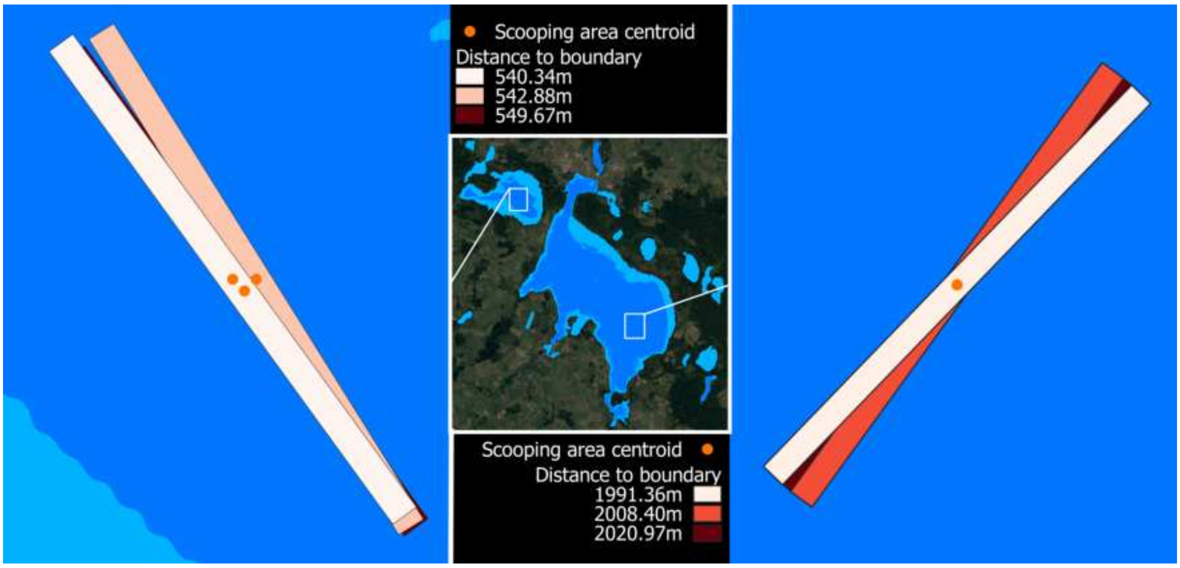

Figure 5.5: On the left, the three best scooping areas are shown for an applicable waterbody whose point of inaccessibility does not fulfill the distance criterion. On the right, the three best scooping areas are shown for an applicable waterbody whose point of inaccessibility does fulfill the distance criterion. The scooping areas are colored according to their minimum distance to the boundary of the waterbody.

The last step is to sort all found scooping areas per waterbody by their minimum distance to the boundary of the waterbody and only keep the ones with the greatest distance. The amount of kept scooping areas per waterbody is defined by the parameter *N*. In the chosen *AOI*, three of the four waterbodies that remained after the waterbody shape filtering described in chapter 5.2.2 can contain at least one scooping area, whereat the best one is visualized (see figure 5.3n). Exemplarily, the three best scooping areas for the two of the three applicable waterbodies within the *AOI* are shown in figure 5.5.

The search algorithm design is discussed in chapter 7.1.2.

5.2.4 Checking for Free Flight Corridors

Last but not least, it needs to be checked if the scooping areas found in chapter 5.2.3 are approachable by airplane. All the principle variables needed in this check are described below.

Flight corridor length: Length of the approaching and the exiting flight corridor to and from the scooping area that is checked if it is free of obstructions. In the scope of this thesis, the *flight corridor length* amounts to 2000m.

Approach / launch angle: This number defines the minimum angle between the approach angle to and the launch angle from the scooping area of the airplane. It is used to check if the flight corridors are free of obstructions depending on the distance to the scooping area. For this thesis, a conventional angle of 3° was assumed as standard.

For each scooping area, the location of flight corridors is calculated. This is done by extending the scooping area with the *flight corridor length* beyond its shorter side in both directions. Next, the Copernicus DEM GLO-30 (see chapter 4.2.2) is loaded for the extent of the scooping area and its flight corridors. The height of the scooping area is taken from this. Afterwards, a proximity raster with the same raster spacing as the loaded DEM is created which contains the distance to the scooping area for each pixel. To determine the maximum permitted height of the surface for each pixel so that an airplane can still approach and launch from the scooping area, the following formula is used:

$$Permitted\ height_{max} = Proximity_{\ to\ scooping\ area} \times tan(\angle_{airplane}) + height_{scooping\ area} \quad (5.1)$$

whereas $\angle_{airplane}$ is the *Approach / launch angle*. To check, if the Earth's surface beneath the flight corridor fulfills the maximum permitted height, the DEM is subtracted from it. In the final raster, positive height differences indicate a free flight corridor, negative height difference indicate the opposite. If the flight corridors of a scooping area are not completely free, the respective scooping area is omitted from the final collection of scooping areas in the AOI. The check of the flight corridors is exemplarily visualized for one of the waterbodies in the AOI in figure 5.3o. The shown scooping area is omitted from the final result (see figure 5.3p) because the flight corridors are not completely free of obstructions.

6 Results

The methodology was applied in the German states Mecklenburg-Vorpommern and Bavaria in July 2024. For both AOIs, all variables were set to the default values presented in the previous chapter. In Mecklenburg-Vorpommern, water areas deeper than 3m were extracted from the depth maps for Mecklenburg-Vorpommern dataset (see chapter 4.1.1). In Bavaria, the depth information was retrieved from the depth segmentation explained in chapter 5.1.

In the following, at first, the results of the training of the depth segmentation model (see chapter 5.1.1) are presented, and secondly, the results of the scooping area search in Mecklenburg-Vorpommern and Bavaria are shown.

6.1 Depth Segmentation Model Training Results

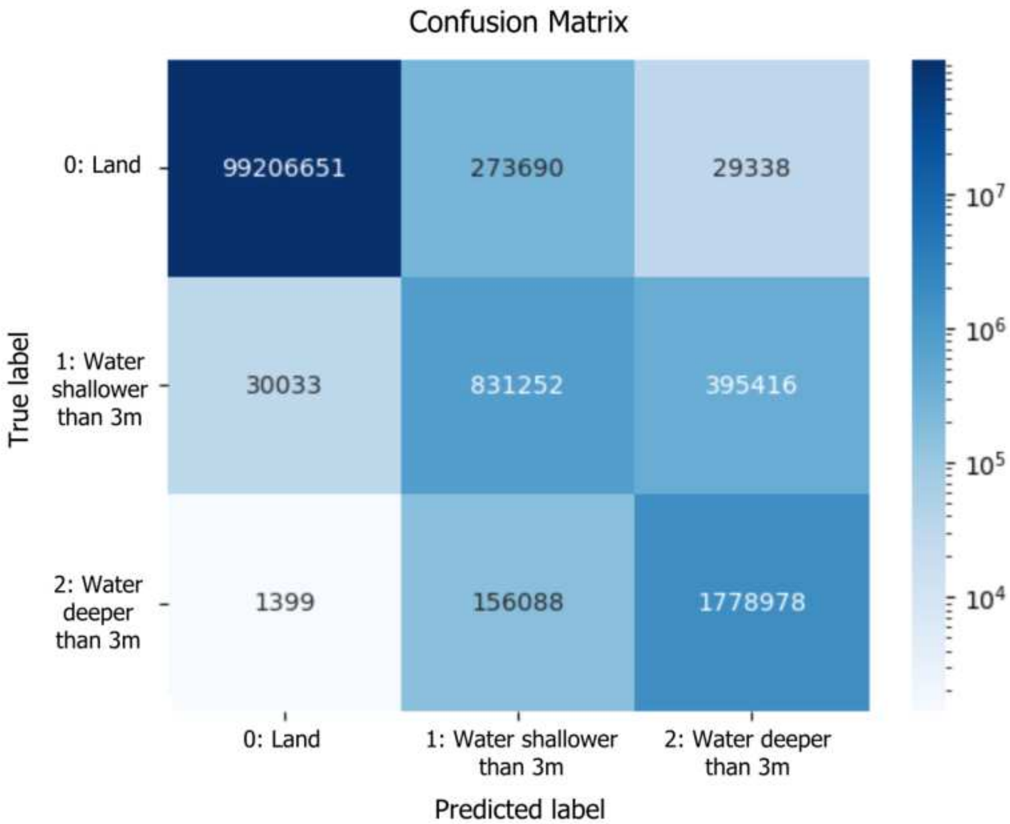

Figure 6.1: Confusion matrix of depth segmentation model with absolute values.

After training the depth segmentation model, which is an adaption of the *DLRS2-Water-Processor* model introduced in chapter 4.2.1, it was tested on the independent test split. The confusion

Metrics	Classes		
	0: Land	**1: Water shallower than 3m**	**2: Water deeper than 3m**
IoU	0.997	0.493	0.753
Precision	1	0.659	0.807
Recall	0.997	0.661	0.919

Table 6.1: The table shows the metrics IoU, precision, and recall calculated from the confusion matrix in figure 6.1 for the three classes *land*, *water shallower than 3m*, and *water deeper than 3m*.

matrix (see figure 6.1) and the metrics derived from it (see table 6.1) show that the model is still proficient in differentiating between land and water, which was its core task before its adaption to also differentiate between water shallower and deeper than 3m. The precision of the *land* class is 1.0, meaning that virtually all pixels the model classified as *land* were in fact part of class *land*. Its recall is 0.997 meaning that 99.7% of class *land* was correctly identified by the model. This yields an IoU of 0.997.

The prediction of class *water deeper than 3m* reached a precision of 0.807. 17.9% of the *water deeper than 3m* predictions were in fact false positives and belonged to class *water shallower than 3m*. 91.9% of the pixels belonging to *water deeper than 3m* were correctly identified by the model. In total, the IoU of class *water deeper than 3m* yields 0.753.

The prediction of class *water shallower than 3m* reached a recall of 0.661, meaning that 66.1% of this class was correctly identified by the model. 31.5% of the true labels of *water shallower than 3m* were in fact false negatives and incorrectly classified as class *water deeper than 3m*. 65.9% of the pixels classified as *water shallower than 3m* were correctly assigned by the model. Overall, the IoU of class *water shallower than 3m* yields 0.493.

6.2 Mecklenburg-Vorpommern

In Mecklenburg-Vorpommern, SAFER detected 368 inland waterbodies bigger than 0.2km² with a total area of 771.83km². After applying the filters mentioned in chapter 5.2.2, 41 waterbodies with an total area of 235.45km² remained. In the end, only nine of them are large and deep enough to contain a scooping area with the dimensions 2000m × 100m × 3m for which the surrounding topography allows airplanes to approach them and launch from them. For each waterbody, the best scooping area, meaning the one that is the furthest from the boundary of the waterbody, is outputted and visualized in figure 6.2. These are:

- Plauer See
- Schweriner See
- Fleesensee
- Kölpinsee
- Müritz
- Krakower See
- Tollensesee
- Woblitzsee
- Torgelower See

SAFER even found nine more inland waterbodies that are able to contain a scooping area, but they are not approachable by an airplane with attack / launch angle of 3° due to the surrounding topography. These are:

- Cambser See
- Ziegelsee
- Tiefwarensee
- Großer Labussee
- Drewensee
- Nebel
- Rätzsee
- Vilzsee
- Labussee

The depth information of the inland waterbodies came from the depth maps of the lakes in Mecklenburg-Vorpommern dataset (see chapter 4.1.1), meaning that no depth segmentation according to chapter 5.1.2 was performed because the dataset was already used as training data for the depth segmentation model (see chapter 5.1.1).

6.3 Bavaria

In Bavaria, SAFER detected 246 inland waterbodies bigger than 0.2km² with a total area of 757.56km². After applying the filters mentioned in chapter 5.2.2, 41 waterbodies with an total area of 238.51km² remained. In the end, only eleven of them are large and deep enough to contain a scooping area with the dimensions 2000m $\times$ 100m $\times$ 3m for which the surrounding topography allows airplanes to approach them and launch from them. For each waterbody, the best scooping area, meaning the one that is the furthest from the boundary of the waterbody, is outputted and visualized in figure 6.3. These are:

- Bavarian part of Lake Constance
- Ammersee
- Wörthsee
- Starnberger See
- Staffelsee
- Großer Brombachsee
- Wagigner See
- Chiemsee
- Simssee
- Forggensee
- Tegernsee

SAFER even found four more inland waterbodies that are able to contain a scooping area, but they are not approachable by an airplane with attack / launch angle of 3° due to the surrounding topography. These are:

- Kochelsee
- Walchensee
- Sylvenstein Reservoir
- Danube river east of the Danube dam in Ingolstadt

The depth information of the inland waterbodies came from the depth segmentation model (see chapter 5.1.1) whose inference was executed by Sentinel-2 MSI Level 3A (MAJA/WASP Tiles) for Germany (see chapter 4.1.2) scenes for July 2024.

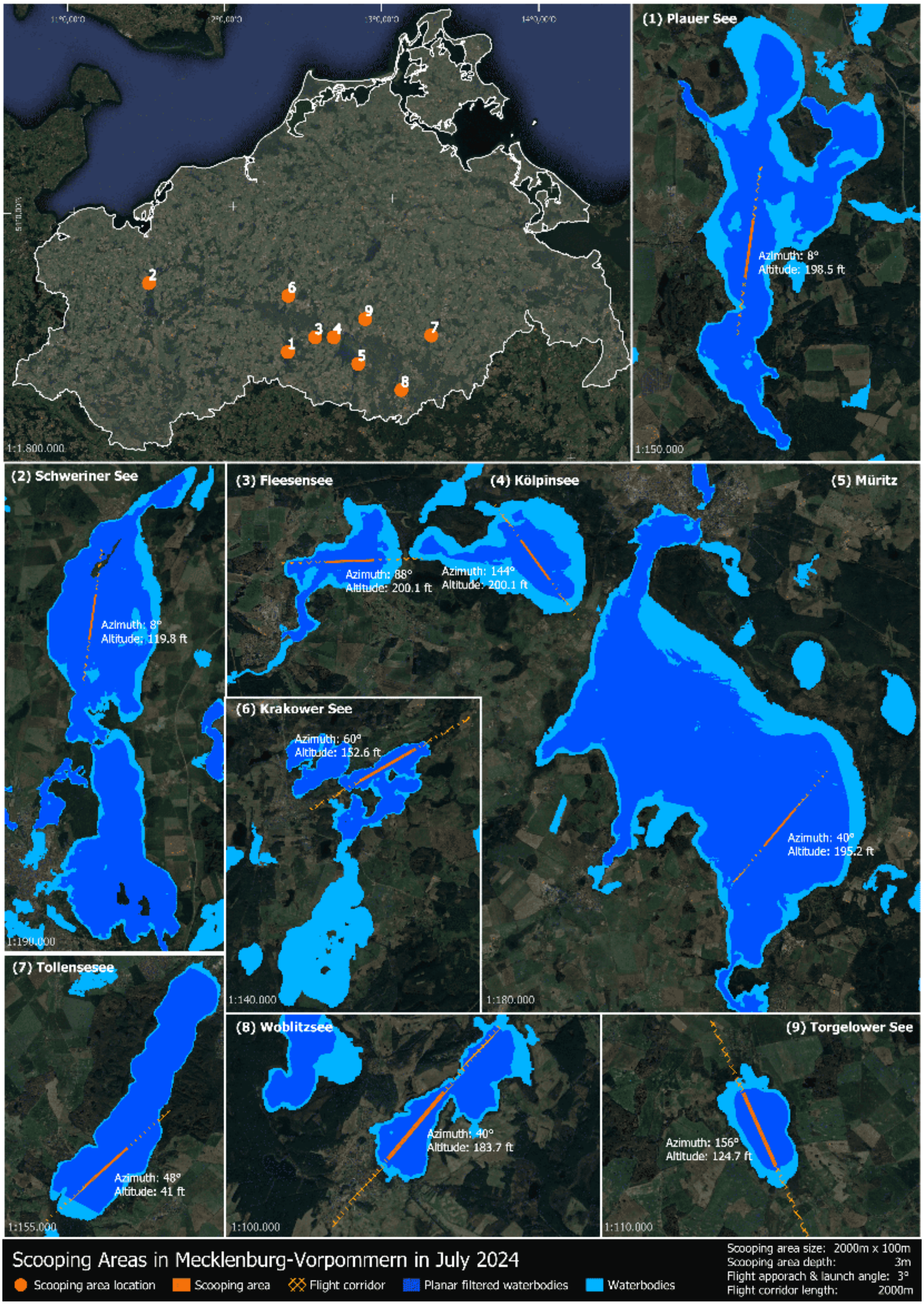

Figure 6.2: The image shows the best scooping area for each waterbody that is able to contain scooping areas in Mecklenburg-Vorpommern for July 2024. In the upper left corner, an overview map of the AOI is given. Planar filtered waterbodies are either part of a nature reservoir or not deeper than 3m.

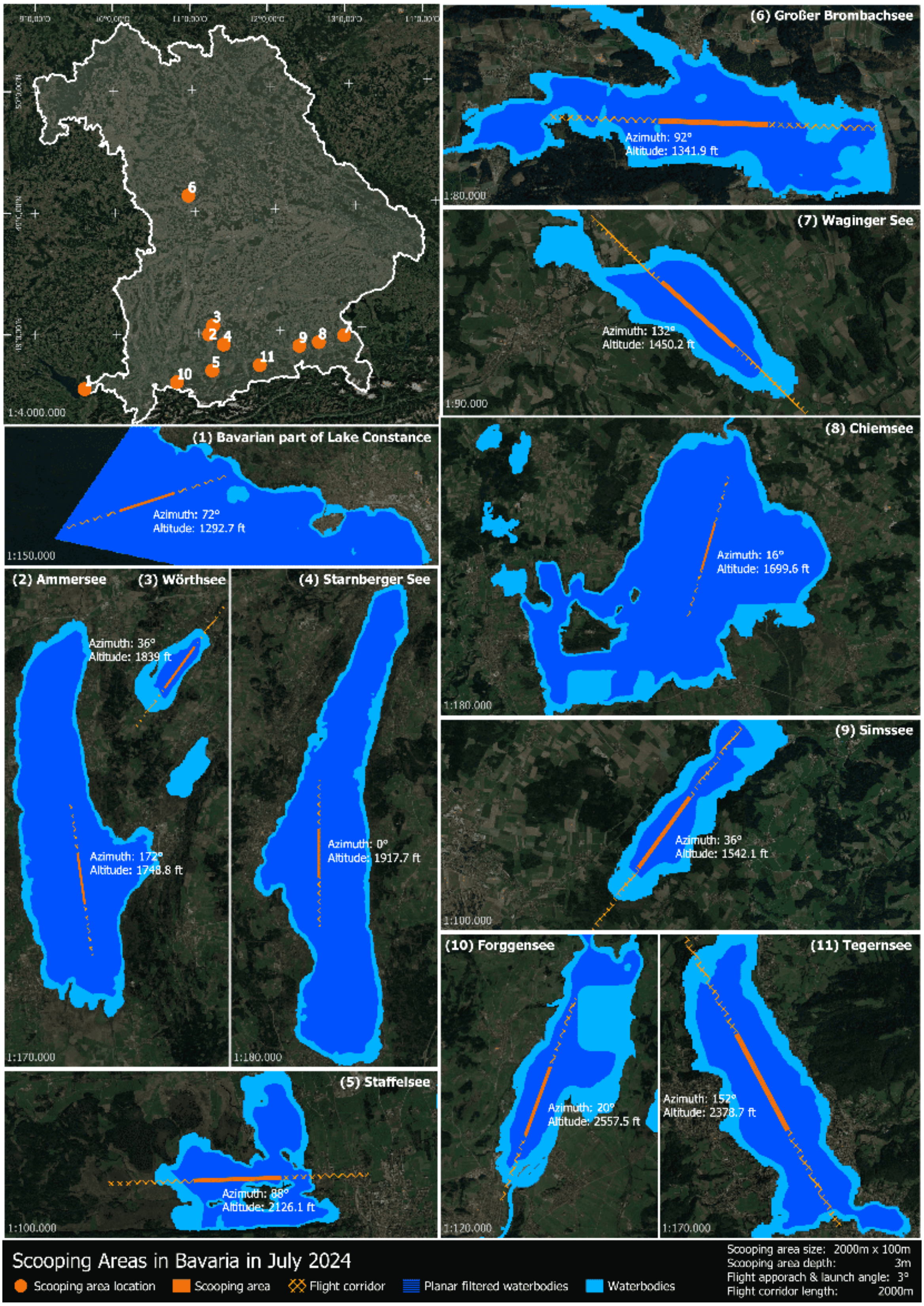

Figure 6.3: The image shows the best scooping area for each waterbody that is able to contain scooping areas in Bavaria for July 2024. In the upper left corner, an overview map of the AOI is given. Planar filtered waterbodies are either part of a nature reservoir or not deeper than 3m.

7 Discussion

The results in the previous chapter have shown that it is feasible to efficiently identify inland waterbodies that are able to contain scooping areas using EO data and shape filtering analysis. Furthermore, this thesis proposed a distance criterion to rank the found scooping areas per waterbody and find the optimal ones. Additionally, it showed that it is at least generally possible to classify water surfaces of inland waterbodies whether they are deeper or shallower than 3m solely based on EO data. And last but not least, it successfully applied height information to check if the flight corridor for firefighting planes to and from the scooping area is free of obstructions.

In the following, the above answers of the research questions from chapter 1.3 are elaborated in more detail.

7.1 Efficiency of the Identification of Inland Waterbodies and Scooping Areas

For the evaluation of the efficiency of SAFER, the quality of the detection of scooping areas and its runtime is discussed in the following.

7.1.1 Quality of DLRS1S2-Water-Processor

First and foremost, the quality of the output of SAFER depends on the quality of the underlying water mask, which is generated from the DLRS1S2-Water-Processor dataset by a monthly median-aggregation of all the individual DLRS1S2-Water-Processor tiles, based on Sentinel-1 and Sentinel-2, as described in chapter 5.2.1. However, the detection rate of water by the *DLRS2-Water-Processor* model is heavily dependent on the cloud cover Wieland et al. [2024]. Hence, for DLRS1S2-Water-Processor tiles based on Sentinel-2, a maximum cloud cover of 25% was chosen in the scope of this thesis balancing the reduced availability of Sentinel-2 scenes per month with its detectable water area in Germany. In figure 7.1a, the variability of available Sentinel-2 scenes per month in whole Mecklenburg-Vorpommern depending on the cloud cover can be seen. The availability of Sentinel-2 scenes with a maximum cloud cover of 25% ranges within a two-year span from roughly ten in January 2021 to almost 130 in March 2022. Consequently, the variability of available Sentinel-2 scenes can also be reflected in the water area solely detected by DLRS1S2-Water-Processor tiles based on Sentinel-2. In the example of the two-year span in Mecklenburg-Vorpommern, figure 7.1b shows a detected water area of less than 2000km^2 in January 2021, while in March 2022, it yields almost 16000km^2. The user of SAFER is able to adapt the maximum cloud cover for Sentinel-2 tiles.

To stabilize the strong variability of detected water area solely based on Sentinel-2 scenes, the DLRS1S2-Water-Processor tiles based on Sentinel-1 are also included in the monthly median-aggregation of the individual water masks. Due to Sentinel-1's independence of the atmosphere's

Figure 7.1: In a), the platform availability per month is shown for the DLRS1S2-Water-Processor dataset in Mecklenburg-Vorpommern between January 2020 and December 2022. Only Sentinel-2 scenes with a maximum cloud coverage of 25% are counted. In b), the water area detected in the scenes from a) and median-aggregated per month are shown.

condition, figure 7.1b shows an approximate constant detected water area solely based on Sentinel-1 scenes over the whole two-year span, which also reflects the approximate constant detected water area by median-aggregating both Sentinel-1 and Sentinel-2 scenes from the DLRS1S2-Water-Processor dataset. This could make it seem that the DLRS1S2-Water-Processor tiles based on Sentinel-2 are dispensable. However, they are kept in the monthly median-aggregation due to two reasons. Firstly, their underlying model has a better performance with less false negative and false positive predictions than the underlying model of the DLRS1S2-Water-Processor tiles based on Sentinel-1 (see chapter 4.2.1). The former model is credited with an IoU of 0.962, while the latter has an IoU of merely 0.838. Secondly, since January 2022, there are less Sentinel-1 scenes available per month, which could reduce the quality of the monthly median-aggregation. The decline of available Sentinel-1 scenes in January 2022 is also observable in figure 7.1a. This is because one of the two Sentinel-1 satellites, Sentinel-1B does not deliver radar data since 23rd December 2021 because it experienced sudden difficulties with the instrument electronics power supply Copernicus [2024c]. Nonetheless, Sentinel-1C is expected to take over in the end of 2024 Copernicus [2024b].

7.1.2 Shape Filtering and Fitting Algorithm

After the application of the data-dependent shape filters on the detected waterbody polygons, the best way to omit remaining waterbody polygons which are not able to contain scooping areas is to find the largest inscribed rectangle with arbitrary orientation of each remaining waterbody polygon and check for its dimensions being smaller than the dimensions of a scooping area. However, in all conscience, there is no such applicable algorithm (see chapter 2.2). Hence, SAFER uses the closest alternative by calculating the minimum oriented bounding box instead and comparing its dimensions to the ones from a scooping area. However, after applying this filter, it is still possible that waterbody polygons that are not able to contain a scooping area remain as input to the shape fitting algorithm, which might increase the runtime of SAFER.

In all conscience, there are also no shape fitting algorithms applicable to this thesis' objective (see chapter 2.2), searching for all the scooping areas that fit inside the remaining shape-filtered waterbodies. Therefore, SAFER applied an iterative brute-force search for scooping areas by trying different locations and rotations of a scooping area. However, to drastically reduce the runtime of this iterative brute-force search, remaining waterbodies were split in two categories according to the distance of the point of inaccessibility of a waterbody to its boundary (see chapter 5.2.3).

Often, large waterbodies do fulfill the distance criterion of their point of inaccessibility, restricting the iterative search for scooping areas to this exact point. It prevents the shape fitting algorithm to loop over different locations within larger waterbodies, reducing the computing time. Furthermore, it guarantees to find the best scooping areas within a waterbody according to this thesis' definition (see chapter 5.2.3), reducing the chance of not being able to approach them by firefighting airplane because of the point of inaccessibility's large distance to the boundary of the waterbody. Also, the categorization is independent of a fixed parameter defining the size of a waterbody. However, a scooping area in the point of inaccessibility does not always entail free flight corridors. The approach is unadaptable to find potential scooping area spots within comprehensive waterbodies that seem to be ideal, not because of their distance to the boundary, but because of the flat surrounding topography guaranteeing free flight corridors.

Waterbodies that do not fulfill the distance criterion of their point of inaccessibility are often smaller, meaning that a full on brute-force iteration over location and rotation of a scooping area is reasonable.

7.1.3 Control of Quality and Runtime

The quality of the result and the runtime of SAFER are codependent. If the search is conducted more thoroughly, the runtime of SAFER will increase, and the other way around. This balance is mainly (not exclusively) influenced by the choice of three principle variables, namely *water mask GSD*, *dTranslation*, and *dRotation*, which are all defined in chapter 5.2. The former influences the runtime of the polygonization of the aggregated water mask, the two latter variables influence the runtime of the shape fitting algorithm.

In table 7.1, the influence of the three above mentioned variables on the runtime and the quality of the result is depicted in three different scenarios for two different AOIs (Bavaria and Mecklenburg-Vorpommern). Exemplarily, Bavaria was covered by 14 smaller grid tiles, while Mecklenburg-Vorpommern was covered by just one grid tile.

AOI	Water mask GSD	# of waterbodies		Water area [km²]		dT	dR	Found water-bodies	Time
		Before filter	After filter	Before filter	After filter				
BY (14 grid tiles)	30	246	26	757.56	238.51	30	4	11	44min
	30	246	26	757.56	238.51	60	8	11	39min
	60	303	26	892.60	238.45	60	8	11	21min
MV (one grid tile)	30	368	41	771.83	235.45	30	4	9	89min
	30	368	41	771.83	235.45	60	8	7	19min
	60	414	41	851.75	235.63	60	8	7	12min

Table 7.1: Performance of SAFER for returning the best scooping area per waterbody depending on the AOI (BY for Bavaria using 14 grid tiles, MV for Mecklenburg-Vorpommern using one grid tile), the number of detected waterbodies (# of waterbodies), the water area, the dTranslation parameter from the iterative grid search (dT), the dRotation parameter from the iterative rotation (dR), and the GSD of the water mask. The runtime is based on running SAFER on a NVIDIA RTX A4000 GPU.

Generally, it is shown that the lower the three variables, the more waterbodies that are able to contain a scooping area are found and the higher the runtime. In Mecklenburg-Vorpommern, doubling *dTranslation*, and *dRotation* effects a decrease of the runtime roughly by the factor of 8, while two waterbodies that are able to contain a scooping area were not identified. For Bavaria, the doubling of *dTranslation*, and *dRotation* only reduced the runtime by about 10% while still identifying the same amount of waterbodies that are able to contain a scooping area. The runtime did not decrease by much in comparison to Mecklenburg-Vorpommern because Bavaria was covered by 14 grid tiles meaning that the majority of the runtime was used to polygonize the 14 water masks which is not influenced by the two changed variables. The number of identified waterbodies that are able to contain a scooping area did not change because in Bavaria, on average larger waterbodies remained after filtering than in Mecklenburg-Vorpommern, meaning that a more coarse brute force search can deliver the same results. When additionally doubling the GSD of the aggregated water mask and thereby reducing the runtime of the water mask polygonization, the total runtime of Bavaria almost halved. In Mecklenburg-Vorpommern, the total runtime reduced by roughly 35%. Increasing the GSD, however, results in the water mask becoming less accurate, as contiguous waterbodies can suddenly be recognized as divided, and shore areas can be recognized as larger than in reality.

7.1.4 Scalability and Transferability of Application

As an efficient algorithm, SAFER is scalable and transferable.

The input AOI to SAFER can also be a grid with overlapping tiles covering the whole AOI, making it possible to apply SAFER to extensive areas without causing memory problems.

The input AOI to SAFER is transferable to every location on Earth that is covered by the two main datasets of SAFER, namely DLRS1S2-Water-Processor (see chapter 4.2.1) and the Copernicus DEM GLO-30 (see chapter 4.2.2), both of which are globally available. However, the input data for the data-dependent filtering (see chapter 5.2.2) needs to be acquired by the user beforehand, including the depth information for all waterbodies. When using the depth segmentation approach introduced in chapter 5.1 for transferring the depth information outside of Germany, another data input to the depth segmentation model needs to be chosen because the Sentinel-2 MSI Level 3A (MAJA/WASP Tiles) for Germany dataset used in the scope of this thesis is only available in Germany (see chapter 4.1.2). Valid alternatives are presented by Theia [2024].

7.2 Ranking of Detected Scooping Areas

Given that a large amount of scooping areas can be detected per waterbody (depending on the grid search parameters), it is beneficial to narrow down the choice of scooping areas to maintain an overview and speed up the decision of a scooping area. The results have shown that it is feasible to rank the detected scooping areas per waterbody by a distance criterion, defining that the further a scooping area is from the boundary of its waterbody, the better the scooping area is deemed. For the criterion, the minimum distance between the scooping area polygon and the boundary of the waterbody is calculated. It assumes that a large distance to the boundary of the waterbody indicates a large distance to shallower waters and obstructions in the flight corridors such as vegetation or buildings, which in turn guarantees a safer approach, scoop, and launch of a firefighting airplane.

7.3 Depth Segmentation and Availability of Reference Data

The depth segmentation performed in the scope of this thesis is an attempt to make the three-class differentiation between background (land), shallow water, and deep water applicable on a global scale with a monthly temporal resolution by means of EO data and a CNN segmentation model. As depth threshold between the two water classes, 3m was chosen according to the objective of this thesis defined in 1.2.

In line with the evaluation of the depth segmentation results, the focus is placed on maximizing precision for the class *water deeper than 3m*, where scooping operations are viable, in order to avoid false identifications of non-eligible water areas, as such errors could critically hinder the scooping process of a firefighting airplane. Conversely, for class *water shallower than 3m*, prioritizing recall (meaning that minimal false negatives shall occur) allows for a broader margin of safety for the scooping process of a firefighting airplane. In general, false positives of class *water deeper than 3m* and false negatives of class *water shallower than 3m* whose true labels are in fact *land* are not further regarded. This is because in the current processing pipeline of SAFER, the distinction between water and land is already made in the first processing step with the DLRS1S2-Water-Processor dataset (see chapter 5.2.1), ensuring that misclassifications related to water depth do not extend to non-water areas. As a result, these misclassifications occur only within areas already confirmed to be waterbodies, minimizing the impact on SAFER.

The depth segmentation results achieved by the adapted *DLRS2-Water-Processor* model using the Sentinel-2 MSI Level 3A (MAJA/WASP Tiles) for Germany dataset, evaluated against reference depth data from Mecklenburg-Vorpommern (see chapter 5.1), provide valuable insights into the model's capacity for differentiating between *land*, *water shallower than 3m*, and *water deeper than 3m*, which is crucial for identifying potential scooping areas for aerial firefighting. In general, the model achieved a satisfactory distinction between the three classes. Nonetheless, the results require careful consideration.

For class *water deeper than 3m*, the model achieved a precision of 80.7% and a recall of 91.9%. This high recall indicates that the model was effective in identifying most areas of *water deeper than 3m*, which is essential for conducting scooping processes. However, the precision of 80.7% suggests that 17.9% of the areas predicted as *water deeper than 3m* were false positives belonging to class *water shallower than 3m* that are not actually suitable for scooping area locations. While this is a relatively strong performance, the operational focus on *water deeper than 3m* necessitates reducing these false positives further, as misidentifying non-eligible water areas could pose a risk to the success of scooping attempts by firefighting airplanes.

Conversely, for *water shallower than 3m*, the model's recall was 66.1%, meaning that 66.1% of shallow water areas were correctly identified. The precision was 65.9%, indicating a fairly balanced but moderate performance. However, the recall of 66.1% suggests that 31.5% of class *water shallower than 3m* were incorrectly classified as *water deeper than 3m* potentially leading to an overestimation of water areas that do not meet the depth criteria of 3m. Misclassifying *water shallower than 3m* as *water deeper than 3m* could lead to the placement of scooping areas in water areas that do not meet the 3m depth requirement, posing a significant risk for the scooping attempts by firefighting airplanes.

One possible explanation for the 17.9% false positives for class *water deeper than 3m* and the 31.5% false negatives for class *water shallower than 3m* could be linked to the temporal discrepancy between the training and reference data. The depth maps of lakes in Mecklenburg-Vorpommern used as reference data were collected through measurements conducted between 1993 and 2011 (see chapter 4.1.1), while the training data in form of the Sentinel-2 MSI Level 3A (MAJA/WASP Tiles) for Germany dataset represents the scene from May 2018. This temporal gap could lead to misalignments in water depth classifications, particularly as inland waterbody depths can fluctuate over time due to natural processes such as sedimentation, seasonal changes, or water level management activities. However, the depth maps of lakes in Mecklenburg-Vorpommern dataset was, in all conscience, the only depth dataset of such a large geographical extent that offered

Figure 7.2: Residual cloud patches over waterbodies in the Sentinel-2 MSI Level 3A (MAJA/WASP Tiles) for Germany dataset in Mecklenburg-Vorpommern for May 2018.

high enough depth resolution to be able to differentiate between water deeper and shallower than 3m, which is why this time discrepancy was accepted as a trade-off during the attempt of a depth segmentation. A similar alternative could have been the bathymetry of Lake Constance dataset [Internationale Gewässerschutzkommission für den Bodensee (IGKB), 2015], which is a terrain model of the lake bottom surface. It was created using airborne topobathymetric laserscanning and multibeam echosounder techniques between 2013 and 2014 [Wessels et al., 2015]. However, even though it had been less, it still would have caused temporal discrepancy with respect to the training data. Also, it would have offered depth information for less water area and less spatial variability than the depth maps of lakes in Mecklenburg-Vorpommern dataset. Furthermore, another potential source of error may be related to the quality of the Sentinel-2 MSI Level 3A (MAJA/WASP Tiles) for Germany dataset itself. While WASP is generally effective in minimizing cloud cover and shadows, it is not entirely immune to minor artifacts, especially over water surfaces (see figure 7.2. Such artifacts, including small residual cloud patches or shadowing effects, could distort the reflectance values in the WASP scene, leading to misclassifications of water depth.

Addressing these discrepancies in future research may involve the use of more recent and spatially more variable reference depth datasets or the use of higher-quality optical satellite imagery as training data. After reducing those discrepancies in the depth segmentation, it would be conceivable to combine the identification of waterbodies (see 5.2.1) with the depth segmentation in the first processing step of SAFER.

7.4 Free Flight Corridor Check

This thesis uses height information from a satellite-derived global DEM, namely the Copernicus DEM GLO-30 (see chapter 4.2.2) to check if flight corridors of scooping areas are free so that the scooping area is approachable with a firefighting airplane. The attack / launch angle and the length of the flight corridor that should be checked are variable and dependent on user preferences. On one hand, using a satellite-derived global DEM is advantageous because it offers spatial coverage for most of the Earth's surface with high spatial resolution. On the other hand, satellite-derived global DEMs are susceptible to temporal changes in dynamic landscapes such as vegetation or urban areas due to their low temporal resolution, as their focus lies on spatial coverage and resolution. And, even though the Copernicus DEM GLO-30 offers a high GSD of 30m, it is still too coarse to be able to detect objects obstructing flight corridors such as power lines, power towers, or windmills. However, the free flight corridor check is only intended to provide an initial assessment with the help of EO data as to whether the scooping area is approachable by airplane or not. The final decision on how to approach the scooping area and at what angle lies with the pilot of the firefighting airplane.

8 Conclusion

This thesis demonstrated the feasibility of using Earth Observation (EO) data to comprehensively identify viable scooping areas (2000m length × 100m width × 3m depth) in inland waterbodies where amphibious firefighting airplanes can scoop up water during a touch-and-go maneuver. The main research questions focused on whether it is possible to efficiently identify inland waterbodies capable of containing scooping areas with EO data, select the best ones of those areas by specific criteria, classify suitable scooping zones based on depth, and verify the presence of free flight corridors to and from the scooping areas. Each of these questions was systematically explored, demonstrating the potential of EO data for large-scale scooping area identification.

By employing a Convolutional Neural Network model for depth segmentation based on optical satellite imagery, the study differentiated between water shallower and deeper than 3m, a critical threshold for scooping operations. The model performed well, achieving a precision of 80.7% for the classification of water deeper than 3m, eligible for scooping areas, and a recall of 66.1% for water shallower than 3m, ensuring that most shallow waters were correctly identified to be excluded from viable scooping zones.

The development of the Scooping Area Finder for aerial fire Emergency Response (SAFER) algorithm enabled the efficient identification of scooping areas that meet the defined criteria. Applied to two distinct regions in Germany, Mecklenburg-Vorpommern and Bavaria, the methodology showed promising results, accurately detecting waterbodies with the DLRS1S2-Water-Processor dataset based on Wieland et al. [2024], efficiently filtering them by spatial and dimensional constraints, while searching the remaining waterbodies for scooping areas, filtering out unsuitable ones based on topographic constraints given by the Copernicus Digital Elevation Model GLO-30, and finally selecting the best scooping areas based on their distance to the boundary of their waterbody. In the region of Mecklenburg-Vorpommern, 368 waterbodies larger than 0.2km^2 were identified, and after applying spatial, dimensional and topographic criteria, 9 were deemed suitable for scooping operations. Similarly, in Bavaria, 246 waterbodies larger than 0.2km^2 were detected, with 11 found to meet the scooping requirements.

The results, however, highlighted the challenge of training the depth segmentation model due to the limited availability of high-resolution depth reference data that covers large, diverse areas. Future work should aim to improve the model's performance by incorporating more recent and higher-quality training data, addressing both spatial variability and depth resolution. Additionally, further improvements can be made by optimizing SAFER to enhance its speed and computational efficiency, making it more suitable for large-scale or real-time operations. This can also be achieved by fast parallel processing platforms such as terrabyte [DLR & LRZ, 2024], which is a high performance data analytics platform operated by the German Aerospace Center and the Leibniz Supercomputing Center specialized on EO data processing.

Despite these challenges, this approach has the potential to be scaled globally, monitoring scooping areas across large spatial extents and in monthly steps. This provides valuable insights into optimizing aerial firefighting efforts and supports approaches like those of Chalabi et al. [2024] by ensuring the safe identification of scooping areas.

Bibliography

Agrafiotis, P., Janowski, L., Skarlatos, D., & Demir, B. (2024). MagicBathyNet: A Multimodal Remote Sensing Dataset for Bathymetry Prediction and Pixel-based Classification in Shallow Waters. In *IGARSS 2024 - 2024 IEEE International Geoscience and Remote Sensing Symposium* (pp. 249–253).: IEEE. `https://doi.org/10.1109/igarss53475.2024.10641355`.

Bai, J., Chen, X., Li, J., Yang, L., & Fang, H. (2011). Changes in the area of inland lakes in arid regions of central Asia during the past 30 years. *Environmental Monitoring and Assessment*, 178, 247–256. `https://doi.org/10.1007/s10661-010-1686-y`.

Berkey, J. O. & Wang, P. Y. (1987). Two-Dimensional Finite Bin-Packing Algorithms. *The Journal of the Operational Research Society*, 38(5), 423–429. `https://doi.org/10.2307/2582731`.

Calkin, D. E., Stonesifer, C. S., Thompson, M. P., & McHugh, C. W. (2014). Large airtanker use and outcomes in suppressing wildland fires in the United States. *International Journal of Wildland Fire*, 23, 259–271. `https://doi.org/10.1071/WF13031`.

Casal, G., Monteys, X., Hedley, J., Harris, P., Cahalane, C., & McCarthy, T. (2019). Assessment of empirical algorithms for bathymetry extraction using Sentinel-2 data. *International Journal of Remote Sensing*, 40(8), 2855–2879. `https://doi.org/10.1080/01431161.2018.1533660`.

Chalabi, W., Bombelli, A., & Purdam, G. (2024). The Aerial Firefighting Vehicle Routing Problem. In *International Conference on Research in Air Transportation, ICRAT 2024*. `https://research.tudelft.nl/en/publications/the-aerial-firefighting-vehicle-routing-problem`, Accessed: 2024-10-25.

Chen, Y., Morton, D. C., & Randerson, J. T. (2024). Remote sensing for wildfire monitoring: Insights into burned area, emissions, and fire dynamics. *One Earth*, 7(6), 1022–1028. `https://doi.org/10.1016/j.oneear.2024.05.014`.

Chung, F. R. K., Garey, M. R., & Johnson, D. S. (1982). On Packing Two-Dimensional Bins. *SIAM Journal on Algebraic Discrete Methods*, 3(1), 66–76. `https://doi.org/10.1137/0603007`.

Chuvieco, E. (2020). *Fundamentals of Satellite Remote Sensing: An Environmental Approach*. Boca Raton: CRC Press, third edition. `https://doi.org/10.1201/9780429506482`.

Cian, F., Marconcini, M., & Ceccato, P. (2018). Normalized difference flood index for rapid flood mapping: Taking advantage of eo big data. *Remote Sensing of Environment*, 209, 712–730. `https://doi.org/10.1016/j.rse.2018.03.006`.

Coffman, Jr., E. G., Garey, M. R., Johnson, D. S., & Tarjan, R. E. (1980). Performance Bounds for Level-Oriented Two-Dimensional Packing Algorithms. *SIAM Journal on Computing*, 9(4), 808–826. `https://doi.org/10.1137/0209062`.

Copernicus (2024a). Copernicus DEM - Global and European Digital Elevation Model. `https://doi.org/10.5270/ESA-c5d3d65`. Accessed: 2024-10-25.

Copernicus (2024b). Sentinel-1C arrives in French Guiana. https://www.esa.int/Applications/Observing_the_Earth/Copernicus/Sentinel-1/Sentinel-1C_arrives_in_French_Guiana. Accessed: 2024-10-25.

Copernicus (2024c). SentiWiki. https://sentiwiki.copernicus.eu/web/. Accessed: 2024-10-25.

Cunningham, C. X., Williamson, G. J., & Bowman, D. M. J. S. (2024). Increasing frequency and intensity of the most extreme wildfires on Earth. *Nature Ecology & Evolution*, 8, 1420–1425. https://doi.org/10.1038/s41559-024-02452-2.

Czyż, Z., Karpiński, P., Skiba, K., & Bartkowski, S. (2023). Numerical Calculations of Water Drop using a Firefighting Aircraft. *Applied Computer Science*, 19(3), 47–63. https://doi.org/10.35784/acs-2023-24.

Daniels, K., Milenkovic, V., & Roth, D. (1997). Finding the largest area axis-parallel rectangle in a polygon. *Computational Geometry*, 7(1), 125–148. https://doi.org/10.1016/0925-7721(95)00041-0.

DG-ECHO (2024a). About European Civil Protection and Humanitarian Aid Operations. https://civil-protection-humanitarian-aid.ec.europa.eu/who/about-echo_en. Accessed: 2024-10-25.

DG-ECHO (2024b). EU Civil Protection Mechanism. https://civil-protection-humanitarian-aid.ec.europa.eu/what/civil-protection/eu-civil-protection-mechanism_en. Accessed: 2024-10-25.

DG-ECHO (2024c). Wildfires. https://civil-protection-humanitarian-aid.ec.europa.eu/what/civil-protection/wildfires_en. Accessed: 2024-10-25.

DG-ECHO and DG-JRC (2022). European Forest Fire report: 3 of the worst fire seasons on record took place in the last 6 years. https://civil-protection-humanitarian-aid.ec.europa.eu/news-stories/news/european-forest-fire-report-3-worst-fire-seasons-record-took-place-last-6-years-2022-10-31_en. Accessed: 2024-10-25.

Dilba, D. (2020). Firefighting aircraft and helicopters: The flying fire brigade. https://aeroreport.de/en/aviation/firefighting-aircraft-and-helicopters-the-flying-fire-brigade. Accessed: 2024-10-25.

DLR & LRZ (2024). terrabyte - An innovative platform for exploring the Earth. https://docs.terrabyte.lrz.de/. Accessed: 2024-10-25.

Earth Observation Center of the German Areospace Center (2024). Sentinel-2 MSI - Level 3A (MAJA/WASP Tiles) - Germany. https://gdz.bkg.bund.de/index.php/default/open-data/digitales-landschaftsmodell-1-250-000-ebenen-dlm250-ebenen.html. Accessed: 2024-10-25.

FAO (2024). *The State of the World's Forests 2024*. Rome: FAO. https://doi.org/10.4060/cd1211en.

German Federal Agency for Cartography and Geodesy (2024). Digitales Landschaftsmodell 1:250 000 (Ebenen) (DLM250). https://gdz.bkg.bund.de/index.php/default/open-data/digitales-landschaftsmodell-1-250-000-ebenen-dlm250-ebenen.html. Accessed: 2024-10-25.

Global Forest Watch (2024). Global Fires. `https://www.globalforestwatch.org/dashboards/global/?category=fires`. Accessed: 2024-10-25.

Internationale Gewässerschutzkommission für den Bodensee (IGKB) (2015). IGKB-Tiefenschärfe-Bodensee digitale Geländemodelle mit 10 m und 3 m Auflösung. `https://doi.org/10.1594/PANGAEA.855987`. Accessed: 2024-10-25.

James, T., Schillaci, C., & Lipani, A. (2021). Convolutional neural networks for water segmentation using sentinel-2 red, green, blue (RGB) composites and derived spectral indices. *International Journal of Remote Sensing*, 42(14), 5338–5365. `https://doi.org/10.1080/01431161.2021.1913298`.

Jolly, W. M., Cochrane, M. A., Freeborn, P. H., Holden, Z. A., Brown, T. J., Williamson, G. J., & Bowman, D. M. J. S. (2015). Climate-induced variations in global wildfire danger from 1979 to 2013. *Nature Communications*, 6, 7537. `https://doi.org/10.1038/ncomms8537`.

Kal'avský, P., Petríček, P., Kelemen, M., Rozenberg, R., Jevčák, J., Tomaško, R., & Mikula, B. (2019). The Efficiency of Aerial Firefighting in Varying Flying Conditions. In *2019 International Conference on Military Technologies (ICMT)* (pp. 1–5). `https://doi.org/10.1109/MILTECHS.2019.8870050`.

Kerr, J. M. & Purkis, S. (2018). An algorithm for optically-deriving water depth from multispectral imagery in coral reef landscapes in the absence of ground-truth data. *Remote Sensing of Environment*, 210, 307–324. `https://doi.org/10.1016/j.rse.2018.03.024`.

Khazaei, B., Read, L. K., Casali, M., Sampson, K. M., & Yates, D. N. (2022). GLOBathy, the global lakes bathymetry dataset. *Scientific Data*, 9, 36. `https://doi.org/10.1038/s41597-022-01132-9`.

Knauer, C., Schlipf, L., Schmidt, J. M., & Tiwary, H. R. (2012). Largest inscribed rectangles in convex polygons. *Journal of Discrete Algorithms*, 13, 78–85. `https://doi.org/10.1016/j.jda.2012.01.002`.

Landuyt, L., Van Wesemael, A., Schumann, G. J.-P., Hostache, R., Verhoest, N. E. C., & Van Coillie, F. M. B. (2019). Flood Mapping Based on Synthetic Aperture Radar: An Assessment of Established Approaches. *IEEE Transactions on Geoscience and Remote Sensing*, 57(2), 722–739. `https://doi.org/10.1109/TGRS.2018.2860054`.

Lumban-Gaol, Y. A., Ohori, K. A., & Peters, R. Y. (2021). Satellite-derived Bathymetry using Convolutional Neural Networks and Multispectral Sentinel-2 Images. *The International Archives of the Photogrammetry, Remote Sensing and Spatial Information Sciences*, XLIII-B3-2021, 201–207. `https://doi.org/10.5194/isprs-archives-XLIII-B3-2021-201-2021`.

Mabula, M. J., Kisanga, D., & Pamba, S. (2023). Application of machine learning algorithms and Sentinel-2 satellite for improved bathymetry retrieval in Lake Victoria, Tanzania. *The Egyptian Journal of Remote Sensing and Space Sciences*, 26(3), 619–627. `https://doi.org/10.1016/j.ejrs.2023.07.003`.

Mandlburger, G., Kölle, M., Nübel, H., & Soergel, U. (2021). BathyNet: A Deep Neural Network for Water Depth Mapping from Multispectral Aerial Images. *Journal of Photogrammetry, Remote Sensing and Geoinformation Science*, 89, 71–89. `https://doi.org/10.1007/s41064-021-00142-3`.

Martinis, S., Twele, A., & Voigt, S. (2009). Towards operational near real-time flood detection using a split-based automatic thresholding procedure on high resolution TerraSAR-X data. *Natural Hazards and Earth System Sciences*, 9(2), 303–314. https://doi.org/10.5194/nhess-9-303-2009.

Marzeh, Z., Tahmasbi, M., & Mirehi, N. (2019). Algorithm for finding the largest inscribed rectangle in polygon. *Journal of Algorithms and Computation*, 51(1), 29–41. https://doi.org/10.22059/jac.2019.71280.

Medium (2020). Convex Hull Algorithms in 2D. https://medium.com/smith-hcv/convex-hull-algorithms-in-2d-976803538452. Accessed: 2024-10-25.

Messager, M. L., Lehner, B., Grill, G., Nedeva, I., & Schmitt, O. (2016). Estimating the volume and age of water stored in global lakes using a geo-statistical approach. *Nature Communications*, 7, 13603. https://doi.org/10.1038/ncomms13603.

Ministerium für Landwirtschaft, Umwelt und Verbraucherschutz M-V, Seenprogramm (2023). Tiefenkarten der Seen in Mecklenburg-Vorpommern. https://www.geoportal-mv.de/portal/Metadatenviewer?mdurl=https%3A%2F%2Fwww.geodaten-mv.de%2Fgeomis%2Fid%2Fe83115b8-a303-4844-8fcd-b77674adacbf. Accessed: 2024-10-25.

Misra, A. & Ramakrishnan, B. (2020). Assessment of coastal geomorphological changes using multi-temporal Satellite-Derived Bathymetry. *Continental Shelf Research*, 207, 104213. https://doi.org/10.1016/j.csr.2020.104213.

Molano, R., Rodríguez, P. G., Caro, A., & Durán, M. L. (2012). Finding the largest area rectangle of arbitrary orientation in a closed contour. *Applied Mathematics and Computation*, 218(19), 9866–9874. https://doi.org/10.1016/j.amc.2012.03.063.

Najar, M. A., Benshila, R., Bennioui, Y. E., Thoumyre, G., Almar, R., Bergsma, E. W. J., Delvit, J.-M., & Wilson, D. G. (2022). Coastal Bathymetry Estimation from Sentinel-2 Satellite Imagery: Comparing Deep Learning and Physics-Based Approaches. *Remote Sensing*, 14(5). https://doi.org/10.3390/rs14051196.

Nolde, M., Plank, S., & Riedlinger, T. (2020). An Adaptive and Extensible System for Satellite-Based, Large Scale Burnt Area Monitoring in Near-Real Time. *Remote Sensing*, 12(13). https://doi.org/10.3390/rs12132162.

Novo, A., Fariñas-Álvarez, N., Martínez-Sánchez, J., González-Jorge, H., Fernández-Alonso, J. M., & Lorenzo, H. (2020). Mapping Forest Fire Risk—A Case Study in Galicia (Spain). *Remote Sensing*, 12(22). https://doi.org/10.3390/rs12223705.

Plucinski, M. (2009). Effectiveness and efficiency of aerial fire fighting in Australia. https://www.bushfirecrc.com/resources/firenote/effectiveness-and-efficiency-aerial-fire-fighting-australia. Accessed: 2024-10-25.

Rösch, M., Nolde, M., Ullmann, T., & Riedlinger, T. (2024). Data-Driven Wildfire Spread Modeling of European Wildfires Using a Spatiotemporal Graph Neural Network. *Fire*, 7(6). https://doi.org/10.3390/fire7060207.

Sarkar, A., Biswas, A., Dutt, M., & Bhattacharya, A. (2018). Finding a largest rectangle inside a digital object and rectangularization. *Journal of Computer and System Sciences*, 95, 204–217. https://doi.org/10.1016/j.jcss.2017.05.006.

Sivrikaya, F., Günlü, A., Ömer Küçük, & Ürker, O. (2024). Forest fire risk mapping with Landsat 8 OLI images: Evaluation of the potential use of vegetation indices. *Ecological Informatics*, 79, 102461. https://doi.org/10.1016/j.ecoinf.2024.102461.

Séries Temporelles (2024). Theia's Sentinel-2 L3A monthly cloud free syntheses. https://labo.obs-mip.fr/multitemp/theias-sentinel-2-l3a-monthly-cloud-free-syntheses/. Accessed: 2024-10-25.

The Infinite Loop (2014). Computing oriented minimum bounding boxes in 2D. https://geidav.wordpress.com/2014/01/23/computing-oriented-minimum-bounding-boxes-in-2d. Accessed: 2024-10-25.

Theia (2024). Sentinel-2 Surface Reflectance. https://www.theia-land.fr/en/product/sentinel-2-surface-reflectance/. Accessed: 2024-10-25.

Thito, K., Wolski, P., & Murray-Hudson, M. (2016). Mapping inundation extent, frequency and duration in the okavango delta from 2001 to 2012. *African Journal of Aquatic Science*, 41(3), 267–277. https://doi.org/10.2989/16085914.2016.1173009.

Traganos, D., Poursanidis, D., Aggarwal, B., Chrysoulakis, N., & Reinartz, P. (2018). Estimating Satellite-Derived Bathymetry (SDB) with the Google Earth Engine and Sentinel-2. *Remote Sensing*, 10(6). https://doi.org/10.3390/rs10060859.

Tyukavina, A., Potapov, P., Hansen, M. C., Pickens, A. H., Stehman, S. V., Turubanova, S., Parker, D., Zalles, V., Lima, A., Kommareddy, I., Song, X.-P., Wang, L., & Harris, N. (2022). Global trends of forest loss due to fire from 2001 to 2019. *Frontiers in Remote Sensing*, 3. https://doi.org/10.3389/frsen.2022.825190.

Wang, X., Liu, H., Tian, Y., Chen, Z., & Cai, Z. (2021). A Fast Optimization Method of Water-Dropping Scheme for Fixed-Wing Firefighting Aircraft. *IEEE Access*, 9, 120815–120832. https://doi.org/10.1109/ACCESS.2021.3106538.

Wessels, M., Anselmetti, F. S., Artuso, R., Baran, R., Daut, G., Gaide, S., Geiger, A., Groeneveld, J. D., Hilbe, M., Möst, K., Klauser, B., Niemann, S., Roschlaub, R., Steinbacher, F., Wintersteller, P., & Zahn, E. (2015). Bathymetry of Lake Constance – a High-Resolution Survey in a Large, Deep Lake. *zfv – Zeitschrift für Geodäsie, Geoinformation und Landmanagement*, 4. https://doi.org/10.12902/zfv-0079-2015.

Wieland, M., Fichtner, F., Martinis, S., Groth, S., Krullikowski, C., Plank, S., & Motagh, M. (2024). S1S2-Water: A Global Dataset for Semantic Segmentation of Water Bodies From Sentinel- 1 and Sentinel-2 Satellite Images. *IEEE Journal of Selected Topics in Applied Earth Observations and Remote Sensing*, 17, 1084–1099. https://doi.org/10.1109/JSTARS.2023.3333969.

Wieland, M. & Martinis, S. (2019). A Modular Processing Chain for Automated Flood Monitoring from Multi-Spectral Satellite Data. *Remote Sensing*, 11(19). https://doi.org/10.3390/rs11192330.

Wu, Z., Mao, Z., & Shen, W. (2021). Integrating multiple datasets and machine learning algorithms for satellite-based bathymetry in seaports. *Remote Sensing*, 13(21). https://doi.org/10.3390/rs13214328.

Xie, H., Luo, X., Xu, X., Pan, H., & Tong, X. (2016). Evaluation of Landsat 8 OLI imagery for unsupervised inland water extraction. *International Journal of Remote Sensing*, 37(8), 1826–1844. https://doi.org/10.1080/01431161.2016.1168948.

Yang, K., Wen, Q., Cheng, Z., & Jia, Z. (2024). Preliminary Study on Wind Tunnel Test of Amphibious Aircraft Dropping Water. In S. Fu (Ed.), *2023 Asia-Pacific International Symposium on Aerospace Technology (APISAT 2023) Proceedings* (pp. 1069–1086). Singapore: Springer Nature Singapore. https://doi.org/10.1007/978-981-97-3998-1_88.

Yang, X., Zhao, S., Qin, X., Zhao, N., & Liang, L. (2017). Mapping of Urban Surface Water Bodies from Sentinel-2 MSI Imagery at 10 m Resolution via NDWI-Based Image Sharpening. *Remote Sensing*, 9(6). https://doi.org/10.3390/rs9060596.

Yunus, A. P., Dou, J., Song, X., & Avtar, R. (2019). Improved Bathymetric Mapping of Coastal and Lake Environments Using Sentinel-2 and Landsat-8 Images. *Sensors*, 19(12). https://doi.org/10.3390/s19122788.